2

NEUTRINO FLUXES FROM COSMIC RAY INTERACTIONS IN THE MILKY WAY

In this chapter two different approaches for estimating the diffuse Galactic neutrino flux are described. The first approach is based on a theoretical modelling of the problem. This requires assumptions about the sources of cosmic rays and their energy spectrum. Also assumptions need to be made about the matter distribution and composition in the Milky Way, since this constitutes the target with which the cosmic rays interact. Finally, assumptions need to be made about the magnetic field in our Galaxy, because the cosmic rays are charged particles and they are influenced by this field. An overview of the relevant properties of the Milky Way and cosmic rays is given in section 2.1. Three different theoretical models are used and these are described and compared in section 2.2.

The second approach to calculate the diffuse Galactic neutrino flux is based on the γ-ray spectrum that is measured by the Fermi satellite. As noted in the previous chapter, these high energy photons are partly created from cosmic ray interactions. The advantage of this approach compared to the theoretical models is that less assumptions have to be made. Only the fraction of the observed photons originating from cosmic ray interactions with the interstellar matter needs to be estimated. This approach is described in section 2.3, and the fluxes obtained in this way are compared to the theoretical fluxes.

Finally, the signal is put into context by comparing it to the main background, which for neutrino telescopes consists of neutrinos produced by cosmic ray interactions in our atmosphere. These so-called atmospheric neutrinos are described in more detail in section 2.4. Finally, the signal fluxes for a neutrino telescope located in the Mediterranean Sea are compared to one located on the South Pole.

2.1 MODEL INGREDIENTS

Before discussing the theoretical models and the underlying assumptions, an overview is given of what is known about the Milky Way and the model ingredients: the interstellar matter, the Galactic magnetic field and cosmic rays.

2.1.1 *The Milky Way*

*Edwin Powell Hubble: *1889; †1953*

Galaxies are classified by their Hubble type [Hubble, 1926], introduced in 1925 by Edwin Hubble. It is normally represented as a tuning-fork diagram, as can be seen from figure 2.1. Most of the galaxies that we know are elliptical, which are denoted by the letter *E* followed by a number that represents the ellipticity, where 0 is nearly circular and 7 is the most ellipse-like. Most of the remaining galaxies are spiral galaxies, of which there are two types: those with a bar (about one-third of the spirals) and those without. The spiral galaxies are denoted by the letter *S* and a second letter (*a*, *b* or *c*) that denotes how tightly wound the spiral arms are, with type *Sa* having the most tightly wound arms. The barred spiral galaxies are denoted with an extra *B* inserted. A few percent of galaxies do not show any regularity. These irregular galaxies are classified as *Irr*. Examples of irregular galaxies are the Magellanic Clouds [Pasachoff, 1979].

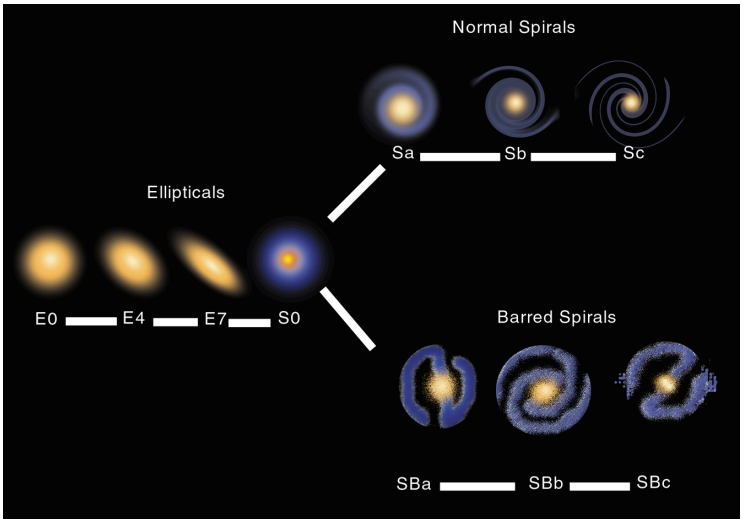

Figure 2.1: The Hubble classification of galaxies. Image credit NASA.

Since the Earth is situated within the Milky Way, it is difficult to classify the Milky Way precisely. It is known that we live in a barred spiral galaxy, but not exactly how tightly wound the spiral arms are. It is thought to be between type *SBb* and *SBc*, also denoted by *SBbc* [Jones and Lambourne, 2004].

The Milky Way, like other galaxies, consists of stars, gas, dust and some form of dark matter. For (barred) spiral galaxies these are organised into a disk (containing the spiral arms), a bulge

and a halo. For elliptical galaxies the disk is not present, they only consist of a bulge and a halo. In the following, the structural components are described in more detail.

The dark-matter halo

The main structural component is the dark-matter halo. The mass of the dark matter is about $10^{12} M_\odot$ (where $M_\odot$ denotes the mass of our Sun: $2 \cdot 10^{30}$ kg). It is primarily the gravity of the dark matter that is responsible for holding the Galaxy together [Pasachoff, 1979]. The dark-matter halo is thought to have the form of a flattened sphere, specifically an oblate spheroid. It is difficult to cite the exact size of the dark-matter halo, since it has not been observed directly. By looking at its effect on the Magellanic Clouds, its diameter is estimated to be at least 100 to 120 kpc.

A parsec (symbol: pc) is the distance from the Sun to an astronomical object having a parallax of one arcsecond and is equal to 3.262 ly.

The disk

Most of the luminous matter is contained in a thin disk, which also contains the Sun and the Earth. Its mass is only one-tenth of the mass of the dark-matter halo ($10^{11} M_\odot$). It consists of stars and the InterStellar Medium (ISM). The ISM contains gas and dust (see section 2.1.2), magnetic fields (section 2.1.3) and cosmic rays (section 2.1.4). Since we are located within the Galactic disk, it appears as a band of diffuse light on the sky.

It is difficult to define *the* radius of the Galactic disk. The stellar disk has an apparent radius of 15 kpc, but the gas and in particular the atomic hydrogen disk extends to about 25 kpc, although the density decreases considerably beyond 15 kpc [Jones and Lambourne, 2004]. The total height of the Galactic disk is about 1 kpc. For an edge-on view of our Galaxy see figure 2.2.

From a bird's-eye view of the Galaxy, the spiral structure is visible, see figure 2.3 for an artist's impression. The spiral arms stand out not because they contain a higher number of stars, but rather since very hot and luminous stars are concentrated there. Our solar system is located near the inner edge of the local Orion-Cygnus arm (Local Arm) at about 8.5 kpc from the Galactic centre and about 15 pc above the midplane [Ferrière, 2001].

The bulge

The density of stars increases towards the centre of the Galaxy and their distribution is more spherical than in the disk. This region is called the bulge and it is thought to have an elongated

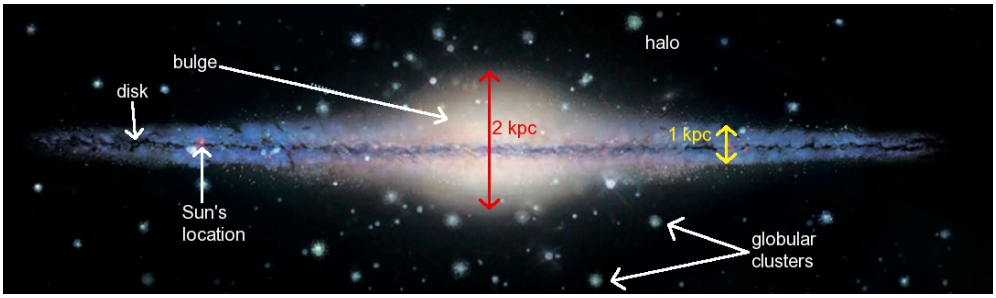

Figure 2.2: Edge-on view of the Milky Way. Figure reproduced after http://woodahl.physics.iupui.edu/Astro105/milkyonedge.jpg.

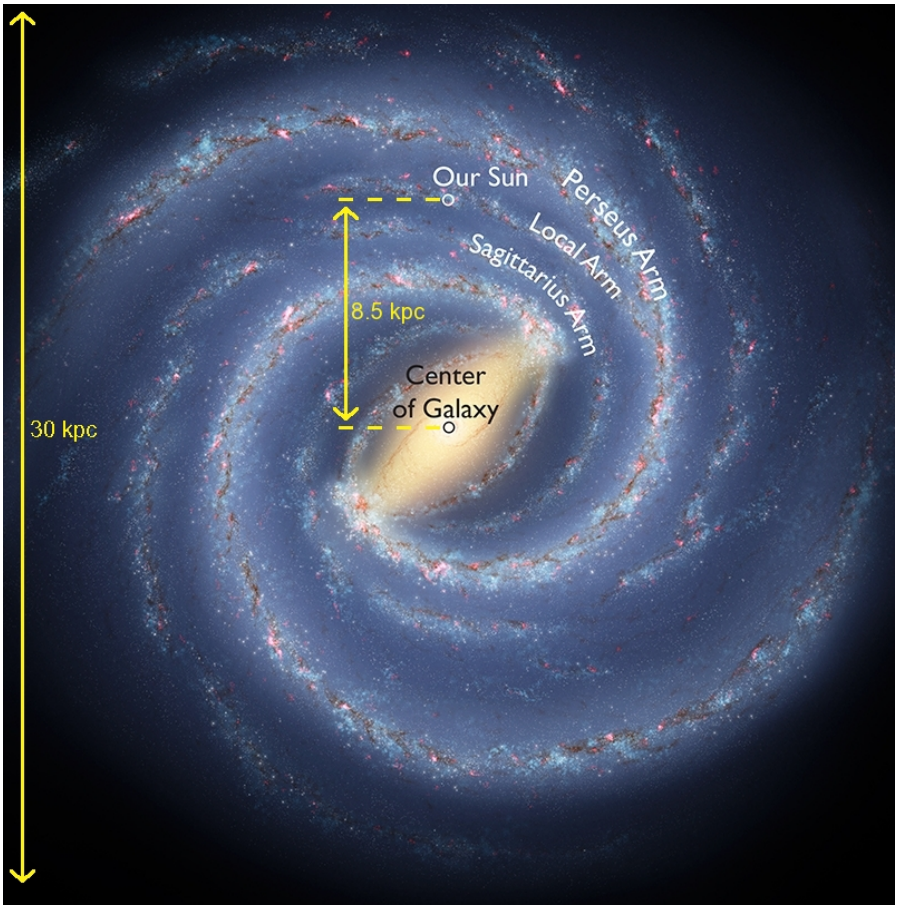

Figure 2.3: Bird's-eye view of the Milky Way. Image credit Robert Hurt, IPAC; Bill Saxton, NRAO/AUI/NSF.

shape, making the Milky Way a barred spiral galaxy. The bulge extends to about 3 kpc on either side of the Galactic centre and has a height (and width) of about 2 kpc.

2.1.2 *The interstellar matter*

The matter in the ISM is made up of gas (in atomic, ionised and molecular forms) and dust. It is concentrated near the Galactic plane (typically found within 150 pc [Jones and Lambourne, 2004] above/below the plane) and in the spiral arms. It has a total mass of about $10^{10} M_{\odot}$. About half of the interstellar mass is confined to clouds which only occupy $1 - 2\%$ of the interstellar volume [Ferrière, 2001]. The chemical composition of the interstellar matter is mainly hydrogen (70.4% by mass, 90.8% by number). Helium makes up 28.1% of the mass (9.1% by number) and the remaining 1.5% of the mass consists of heavier elements (referred to as metals by astronomers). The different forms of matter will now be described separately (for a thorough description of the subject see the lecture notes of Pogge [2011] and the references cited therein).

Neutral atomic gas

The main method of detecting neutral atomic hydrogen (denoted by H I) is via the observation of the 21-cm line, as described in the previous chapter. Only hydrogen is mentioned here since it is the most abundant element in the interstellar matter. The reader should keep in mind the chemical composition described above (see also figure 2.4). The H I is present in two thermal phases:

A. A cold phase with temperatures between 50 and 100 K, located in dense clouds (also called H I regions), with a hydrogen density of $20 - 50\,\mathrm{cm}^{-3}$.

B. A warm phase with temperatures between 6000 and 10000 K, located in the so-called *intercloud medium*, with a hydrogen density of $\sim 0.3\,\mathrm{cm}^{-3}$.

The H I density in the immediate vicinity of the Sun is lower than the values quoted above. It turns out that our solar system is located inside an H I cavity, called the Local Bubble. The Local Bubble has a width of about 100 pc in the Galactic plane and is elongated along the vertical. It is filled with ionised hydrogen (see next section), which has a very low density of only $\sim 0.005\,\mathrm{cm}^{-3}$,

but which has temperatures[1] of nearly 10^6 K. The Local Bubble is carved out by a series of past supernovae [Galeazzi et al., 2014].

As noted before, most of the atomic gas is located in the Galactic disk and is concentrated near the Galactic plane. The exponential scale height of the cold phase is about 100 pc. For the warm phase, two vertical scale height components are seen, one is Gaussian with a scale height of about 300 pc, the other is exponential with a scale height of about 400 pc. However, the disk in which the neutral atomic gas is located is not completely flat. It is only flat and centred around the Galactic plane to distances of about 12 kpc from the Galactic centre, but at greater distances it is tilted, with the gas reaching heights above/below the plane of 1 to 2 kpc [Jones and Lambourne, 2004].

[1] *Actually our solar system is not directly surrounded by the hot gas of the Local Bubble. It is instead located in a warm interstellar cloud, called the Local Cloud, with temperatures of about 6700 – 7600 K and a hydrogen density of about 0.18 – 0.28 cm^{-3}.*

Ionised gas

Ionised hydrogen (denoted by H II) can be detected using the Hα line, which has a wavelength of 656.28 nm. It is one of the Balmer lines and is created when the electron of a hydrogen atom changes its excitation state from $n = 3$ to $n = 2$. The ionised hydrogen is also present in two thermal phases:

*The Balmer lines or Balmer series are named after Johann Jakob Balmer (*1825; †1898), who discovered an empirical formula to calculate them.*

A. A warm phase with temperatures between 6000 and 10000 K, mainly located in the intercloud medium (90%), with a hydrogen density of about 0.1 cm^{-3}, but also partly in H II regions (10%).

B. A hot phase with temperatures above 10^6 K which extends into the Galactic halo, with a very low hydrogen density below about 0.003 cm^{-3}.

The H II regions are created by the UV radiation emitted by hot O and B stars (the most massive and hottest stars in the Milky Way). Inside the H II region, the ions and free electrons continuously recombine, after which the newly created neutral hydrogen will be ionised once more. The size of the region is thus determined by the equilibrium of the recombination rate with the photo-ionisation rate. For an artist's impression of the H I and H II regions see figure 2.4.

The H II regions are highly concentrated along the Galactic plane, with an exponential scale height of about 70 pc, while the diffuse component located in the intercloud medium has an exponential scale height around 1 kpc. For the radial dependence, Cordes et al. [1991] used several different measurements to come to a Gaussian dependence on distance to the Galactic

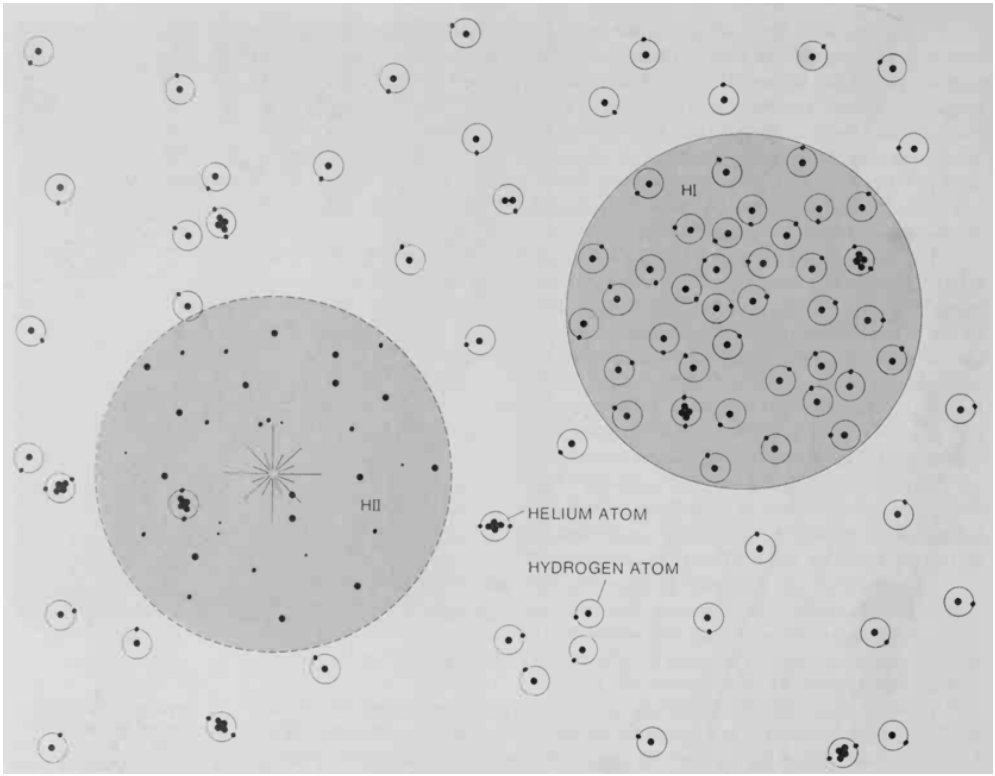

Figure 2.4: Schematic represention of H I and H II regions. Figure reproduced from Pasachoff [1979].

centre with a scale length of 20 kpc, which peaks around 4 kpc, and then decreases again towards the Galactic centre.

The hot interstellar gas is generated by supernova explosions and stellar winds from the progenitor stars. The hot gas is very buoyant and is located in bubbles (like the Local Bubble described above) and fountains that rain back gas on the Galactic disk. Because of this it has a large exponential scale height of about 3 kpc, although the uncertainty on this value is quite large.

Molecular gas

Molecular gas is expected at places where the density is high (as there is a higher chance of atoms meeting each other), the temperature is low (below about 100 K, which avoids collisional disruption) and the UV flux is low (which avoids UV-induced disruption). These are the conditions found in cool dense clouds, which are thus called molecular clouds.

The molecular clouds themselves are organised in complexes with typical sizes between 20 and 100 pc and a mean hydrogen number density between 100 and 1000 cm^{-3}. Cloud complexes are mostly located along the spiral arms and are particularly numerous at distances between 4 and 7 kpc from the Galactic centre.

The most abundant interstellar molecule is H_2. It is difficult to observe this molecule directly, since it has no permanent electric dipole moment and only a very small moment of inertia. Most of what is known about molecular interstellar gas is by the use of so-called *tracers*. The main tracer is the CO molecule (the second most abundant interstellar molecule), which can be observed in its $J = 1 \rightarrow 0$ rotational transition at a radio wavelength of 2.6 mm [Glover and Mac Low, 2011]. The advantage of using radio wavelengths is that the molecular gas itself is transparent to it, so that measurements can be made from the inside of molecular clouds.

Dust

Dust consists of tiny lumps of solid compounds made predominantly of carbon, oxygen and silicon. The typical size of a dust particle is about 0.1 to 1 μm, which makes it comparable in size to the wavelength of visible light. Dust is therefore a very efficient absorber and scatterer of visible light, resulting in the dark lines seen in the top right plot of figure 1.3.

The total mass of the dust is only about 0.1% of the total mass of the stars, but dust is still very important for a number of processes. It serves as a catalyst in the formation of molecular hydrogen and also shields the H_2 against UV light. It is also thought to be important for the formation of planets, since the formation of a planetary system can start with the coagulation of dust grains into planetesimals, which can eventually turn into planets.

Discussion

For the work carried out in this thesis, the H I and H_2 components are the most important constituents of the ISM, with the H II component contributing to a lesser extent. The dust can safely be neglected due to its low density. The hot ionised gas phase can also be neglected, because even though it extends far from the Galactic plane, it has a very low density. It should be noted that according to Taylor et al. [2014], the neutrinos measured by

IceCube might actually originate from PeV cosmic ray interactions in the Galactic halo, after they escape from the Galactic disk.

2.1.3 *The magnetic field*

The observation of the polarisation of starlight from distant stars was the first evidence for the presence of magnetic fields in the ISM [Hiltner, 1949; Hall, 1949]. The polarisation is caused by dust grains, the short axis of which aligns with the local magnetic field. Radiation with the electric field vector parallel to the long axis of the dust grain is mostly absorbed, leading to polarisation along the direction of the magnetic field.

Polarisation measurements only tell us about the direction of the Galactic magnetic field. The strength of the magnetic field can be inferred through other means, such as Zeeman splitting of the 21 cm H I line and Faraday rotation of light from pulsars. See the article of Brown [2011] for an overview of detection techniques.

The magnetic field at our location in the Galaxy has a strength of $3 - 5\,\mu$G [Jansson and Farrar, 2012a], which is very small compared to the typical magnetic field strength at the equator of the Earth of 0.31 G. The Galactic magnetic field consists of two components. A large scale field (also called the regular or uniform component) which evolves slowly and has a local strength of about $1.4\,\mu$G and a small scale field (also called the irregular or random component) representing the fluctuations on the large scale field. These two field components will be described separately.

The regular field

While it is relatively easy to measure the local magnetic field, since it can be measured directly using magnetometers aboard spacecraft, the magnetic field further away in the Galaxy is much more difficult to measure. For this reason there is still some controversy about the exact topology and strength of the magnetic field, but a few properties are widely accepted.

The regular magnetic field component in the disk has a strong azimuthal component and a smaller radial component of which the magnitude is not known. As viewed from the North Galactic pole, the direction of the regular field is clockwise while the direction in the Sagittarius Arm is counter-clockwise. This is the only field reversal that is generally agreed upon, however, it is also possible that there are more magnetic field reversals. There is also still uncertainty about the topology of the regular

field in the disk, and both axisymmetric and bisymmetric spiral configurations (see figure 2.5) are plausible [Haverkorn, 2014]. The strength of the regular field increases smoothly toward the Galactic centre, reaching about 4.4 μG at a radial distance of 4 kpc [Beck, 2008].

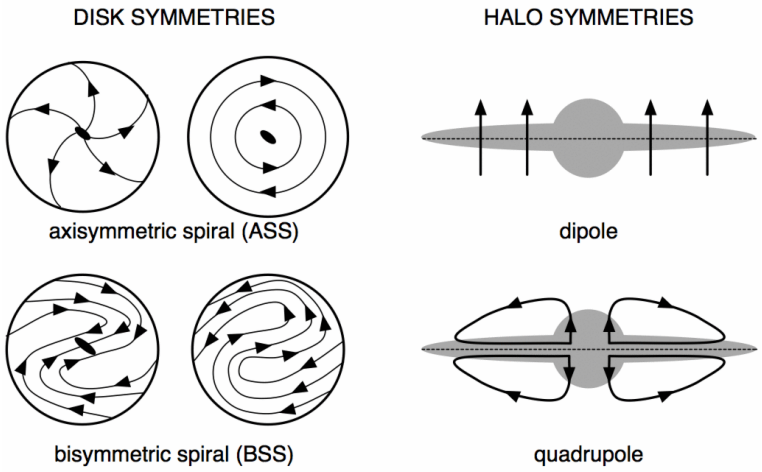

Figure 2.5: The possible configurations of the regular magnetic field in the disk. Figure reproduced from Brown [2011].

The regular field consists of two separate field layers, with one being localised in the disk and the other, which is an order of magnitude weaker than the field in the disk, extending into the Galactic halo. The transition between the layers takes place at a typical distance of 0.4 kpc above/below the Galactic plane [Jansson and Farrar, 2012b]. The exponential scale height of the halo field is about 1.4 kpc. It is not known if the magnetic field in the halo is symmetric above and below the Galactic plane (dipole), or anti-symmetric (quadrupole), see also figure 2.5.

The random field

The random magnetic field, which is associated with the turbulent interstellar plasma, has a local strength of about 5 μG and is also thought to consist of both a disk and a halo component. The strength of the disk component varies per spiral arm and decreases as $1/r$ (with r being the radial distance to the Galactic centre) for radii larger than 5 kpc [Jansson and Farrar, 2012a]. The halo component decreases as an exponential with the radius and is a Gaussian in the vertical direction, with a scale height comparable to the halo component of the regular magnetic field.

The random field has a typical coherence length scale of the order of 100 pc [Prouza and Šmída, 2003].

Discussion

Even though the magnetic field in the halo is an order of magnitude weaker than that in the disk, it is of more importance for the propagation of cosmic rays, since it extends much further in height. Since the strength and scale height of the uniform and random components are of the same order, the transport of cosmic rays in the Galaxy takes place under highly turbulent conditions [Evoli et al., 2007].

2.1.4 *Cosmic ray flux*

As described in the introduction, cosmic rays are charged particles, consisting primarily of protons. The major part of the observed cosmic rays is produced in Galactic sources [Ptuskin, 2012], although there is no consensus yet as to what their origin is. The prime candidates and the acceleration mechanism of cosmic rays are described below. After that, the propagation of cosmic rays through the Galaxy and their interactions with the matter and magnetic fields previously described will be discussed. Some more details will also be given about the cosmic ray fluxes measured at the Earth.

Sources of cosmic rays

SNRs, and the supernova explosions that create them, are the main candidate sources for cosmic rays. There are two types of supernovae: Type I and Type II. Type I supernovae arise when old low-mass stars accrete enough matter from their companion to create a thermonuclear instability. Type II supernovae arise from young stars with a mass of at least $8M_{\odot}$, which go through gravitional core-collapse after all their fuel is exhausted. In both cases a total amount of energy of the order of 10^{46} J is released, of which about 99% is released in the form of neutrinos. The remaining 1% goes into acceleration of interstellar material and electromagnetic radiation (0.01%) [Goobar and Leibundgut, 2011].

There are several theoretical grounds to assume that SNRs are sources of cosmic rays. The relative overabundance of iron points to very evolved early-type stars, which then release the cosmic rays into the ISM in the supernova explosion [Ferrière, 2001]. Also, the shockwaves created by the supernovae are able to accelerate the cosmic rays to higher energies over a broad energy

range and produce the observed power-law energy spectrum (see later in this section). Finally, the amount of energy released in supernova explosions is high enough to maintain a steady cosmic ray energy density [Grupen, 2005].

Recently, the Fermi collaboration claimed the proof that cosmic rays originate from the molecular clouds IC443 and W44, by looking for the characteristic pion-decay feature in the γ-ray spectra [Ackermann et al., 2013] (see also section 2.3.2 for more information). The measurement by Fermi could be the first experimental proof that cosmic rays are indeed accelerated in SNRs.

Concerning the rates of supernovae, there exist big uncertainties. Ferrière [2001] gives a Type I supernova frequency of:

$$f_{\mathrm{I}} \approx \frac{1}{250\,\mathrm{year}}, \tag{2.1}$$

and a Type II supernova frequency of:

$$f_{\mathrm{II}} \approx \frac{1}{60\,\mathrm{year}}, \tag{2.2}$$

in our Galaxy, giving a total rate of about 2 supernovae per century. Other estimates range from 1 to 4 supernova explosions per century.

The spatial distribution of SNRs has also big uncertainties, and various methods exist which yield different results. Besides performing direct measurements of the SNRs, it is also possible to use tracers of supernova explosions. For instance, Type I supernovae are thought to follow the distribution of old disk stars. Pulsars, which result from Type II supernovae, or H II regions, which are produced by the progenitor stars, can be used as tracers of Type II supernovae.

Concerning the radial distribution, Ferrière [2001], gives a distribution for Type II SNRs which consists of a rising Gaussian with a scale length of 2.1 kpc for $r < 3.7$ kpc and a standard Gaussian with a scale length of 6.8 kpc for $r \geqslant 3.7$ kpc. This radial distribution is shown in figure 2.6 as the blue dotted line, together with several other distributions. The differences between the distributions gives a measure for the uncertainty. The vertical distribution of Type II SNRs is given by the superposition of a thin disk with a Gaussian scale height of 0.2 kpc containing 55% of the SNRs and a thick disk with a Gaussian scale height of 0.6 kpc containing the remaining 45%.

For the Type I SNRs, a distribution with an exponential scale length of 4.5 kpc in radius and an exponential scale height of

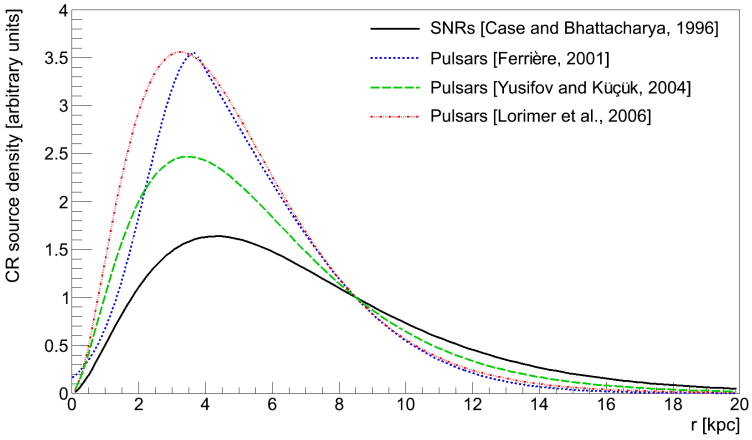

Figure 2.6: Several radial Type II SNR distributions, the legend shows the type of tracer that is used and the reference.

0.3 kpc is obtained from measurements of old disk stars. Although the rate of Type I supernovae is about 4 times lower than that of Type II (compare equations 2.1 and 2.2), the former is more important in the inner Galaxy.

Even though SNRs are the main candidate for the sources of (Galactic) cosmic rays, they might not be the only source. Other cosmic ray candidate sources include pulsars and (for extragalactic cosmic rays) AGNs and GRBs.

GRB: Gamma-Ray Burst, a short but extremely energetic burst of γ-radiation. It is the brightest electromagnetic event known.

Acceleration mechanism

It is generally accepted that primary cosmic rays (those produced in the source) are accelerated further by scattering off moving magnetic field irregularities, regardless of the injection site. This acceleration can happen via the mechanism as proposed by Enrico Fermi, in which cosmic rays interact with magnetic clouds [Fermi, 1949].

*ENRICO FERMI: *1901; †1954*

When a particle of mass m and velocity v is reflected from a magnetic cloud moving with velocity u, the energy gain of the particle is:

$$\Delta E_{\pm} = \frac{1}{2}m(v \pm u)^2 - \frac{1}{2}mv^2, \tag{2.3}$$

where the $+$ $(-)$ sign should be taken when v and u are parallel (anti-parallel). The average net gain of energy is then:

$$\Delta E = \Delta E_{+} + \Delta E_{-} = mu^2, \tag{2.4}$$

which gives a relative energy gain of:

$$\frac{\Delta E}{E} = 2\frac{u^2}{v^2}. \tag{2.5}$$

Since the relative energy gain in equation 2.5 (which is also valid for relativistic velocities) is quadratic in the cloud velocity, this mechanism is called the 2nd order Fermi mechanism. Acceleration by the 2nd order Fermi mechanism will take a very long time, since the cloud velocity is low compared to the particle velocity. Furthermore, the mechanism only works above ~200 MeV, since the energy losses below this energy are larger than the energy gain by the 2nd order Fermi mechanism.

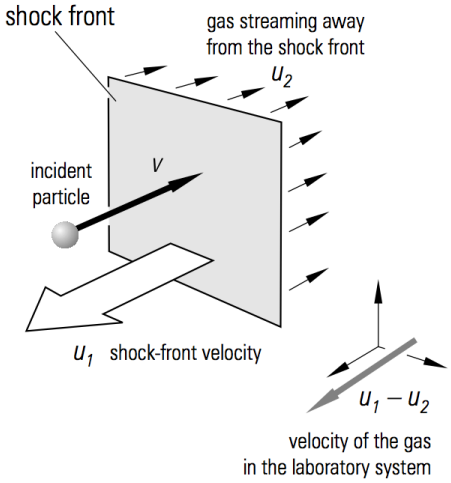

Figure 2.7: Schematic representation of shock acceleration. Figure reproduced from Grupen [2005].

A different mechanism was proposed by Axford et al. [1978], who considered particles colliding with shock fronts (which can be produced by supernova explosions).

Consider a particle colliding with and scattering off a shock front moving with a velocity u_1. Behind the shock front, the gas recedes with a velocity u_2, meaning that the gas has a velocity of $u_1 - u_2$ in the laboratory frame (see figure 2.7). The energy gain of the particle is now:

$$\Delta E = \frac{1}{2}m(v + (u_1 - u_2))^2 - \frac{1}{2}mv^2, \tag{2.6}$$

$$= \frac{1}{2}m(2v(u_1 - u_2) + (u_1 - u_2)^2). \tag{2.7}$$

When considering large particle velocities ($v \gg u_1, u_2$), the first term dominates and the relative energy gain becomes:

$$\frac{\Delta E}{E} = 2\frac{u_1 - u_2}{v}, \tag{2.8}$$

which is linear in the relative velocity, and is thus called the 1st order Fermi mechanism. A relativistic calculation, taking variable scattering angles into account, gives the same dependence on the relative velocity, see Grupen [2005]:

$$\frac{\Delta E}{E} = \frac{4}{3}\frac{u_1 - u_2}{c}. \tag{2.9}$$

The Fermi mechanisms can also explain the observed power-law dependence of the cosmic ray energy spectrum. After one collision/reflection, the particle will have an energy E_1:

$$E_1 = E_0(1 + \epsilon), \tag{2.10}$$

where E_0 is the initial energy and ϵ is the relative energy gain. After n collisions the energy will then be:

$$E_n = E_0(1 + \epsilon)^n. \tag{2.11}$$

Assume now that the probability that the particle escapes (and is not further accelerated) is P_{esc}. After n collisions there will then be:

$$N_n = N_0(1 - P_{\text{esc}})^n, \tag{2.12}$$

particles remaining which have an energy E_n. This results in an energy spectrum given by:

$$\frac{dN}{dE} \propto E^{\frac{\ln(1-P_{\text{esc}})}{\ln(1+\epsilon)}-1}. \tag{2.13}$$

Using the fact that the energy gain per cycle and the escape probability are small (i. e. ϵ, $P_{\text{esc}} \ll 1$) [Grupen, 2005], equation 2.13 can be written as:

$$\frac{dN}{dE} \propto E^{\frac{-P_{\text{esc}}}{\epsilon}-1}. \tag{2.14}$$

An elegant feature of the 1st order Fermi mechanism is that it yields a universal prediction for the spectral index [Baring, 1997]. From kinetic theory, the escape probability for non-relativistic plasma shocks can be written as [Bustamante et al., 2009]:

$$P_{\text{esc}} = \frac{4}{3}\frac{u_1 - u_2}{c}, \tag{2.15}$$

which is identical to the relative energy gain per cycle (equation 2.9), so that equation 2.14 becomes:

$$\frac{dN}{dE} \propto E^{-2}. \tag{2.16}$$

The 2nd order Fermi mechanism also results in a power-law in the energy spectrum, but the spectral index cannot be uniquely determined in this case [Baring, 1997].

It is generally thought that the 1st order Fermi mechanism accelerates particles to a sufficiently high energy, after which they are further accelerated by the 2nd order mechanism.

Transport of cosmic rays

After acceleration, the cosmic ray particles propagate through the interstellar medium under the influence of the interstellar magnetic field. This field confines the cosmic rays to the Galaxy, since they are forced to gyrate about the magnetic field lines, following a circular orbit with radius:

$$r_L = \frac{p}{qB}, \tag{2.17}$$

called the Larmor radius, where B is the magnetic field strength, p is the particle momentum and q its charge. It is useful to rewrite equation 2.17 using $q = Ze$, with Z the atomic number and $e = 1.602 \cdot 10^{-19}\,\mathrm{C}$:

$$r_L = 1.08 \cdot 10^{-6}\,\mathrm{pc}\,\frac{p\,[\mathrm{GeV}/c]}{ZB\,[\mu\mathrm{G}]}, \tag{2.18}$$

in which different units, which are more suited for the situation at hand, are used for the variables.

Inserting the average strength of the magnetic field in the Milky Way of about 3 μG in equation 2.18 gives a Larmor radius of 0.36 pc for a proton ($Z = 1$) with an energy[2] of 10^6 GeV, and 360 pc for a proton with an energy of 10^9 GeV. From these considerations it can be seen that cosmic rays with energies up to at least about 10^7 GeV are contained in the Galaxy.

[2] *At the given energies, energy and momentum are approximately the same, since* $E = \sqrt{p^2c^2 + m^2c^4} \approx pc$ *for a proton mass of* $0.938\,\mathrm{GeV}/c^2$.

In the direction parallel to the magnetic field lines, the cosmic ray particles diffuse through the Galaxy due to the random component of the magnetic field. This component is coherent over length scales of about 100 pc, which is small compared to the size of the Milky Way. This explains the isotropy and relatively long confinement time in the Galaxy (which is inferred from unstable isotopes, see below). Besides diffusion, convection can also play

a role in the transport of cosmic rays, which is inferred from the observation of galactic winds in many galaxies [Strong et al., 2007].

During propagation through the Galaxy, cosmic rays can interact with constituents of the Milky Way in several ways. Some cosmic rays interact with the interstellar matter and produce secondary particles in inelastic collisions. This is the process responsible for the photon and neutrino production, which will be described in detail in sections 2.2 and 2.3. Cosmic ray nuclei can also break up in lighter nuclei like Li, Be and B (referred to as the *light elements*) in collisions with the interstellar gas. This process is known as spallation. As a result, the abundance of light elements in cosmic rays exceeds the average solar system abundances of these elements. The spallation process is the main way in which these light elements are produced [Lemoine et al., 1998] and most of the knowledge about cosmic ray propagation comes from measurements of their abundances. In addition, unstable secondary nuclei are produced, such as ^{10}Be, which is used to deduce the average cosmic ray lifetime.

Spallation is so named because 'spall' is produced: flakes of a material broken off a large solid body due to impact or stress.

Besides losing energy, the cosmic ray particles can also gain energy by scattering off shock fronts or randomly moving magnetic waves. This process can be represented as diffusion in momentum space, and is known as diffusive reacceleration.

In the most general form, the cosmic ray transport can be formulated as [Strong et al., 2007]:

$$\frac{\partial \Phi(\vec{r}, p, t)}{\partial t} = Q(\vec{r}, p, t) + \vec{\nabla} \cdot \left(\mathbb{D}_{xx} \vec{\nabla} \Phi \right) - \vec{\nabla} \cdot \left(\vec{V} \Phi \right) + \frac{\partial}{\partial p} \left(p^2 D_{pp} \frac{\partial}{\partial p} \frac{\Phi}{p^2} \right) - \frac{\partial}{\partial p} \left[\frac{\partial p}{\partial t} \Phi - \frac{p}{3} \left(\vec{\nabla} \cdot \vec{V} \right) \Phi \right] - \frac{\Phi}{\tau_f} - \frac{\Phi}{\tau_d}, \tag{2.19}$$

where $\Phi(\vec{r}, p, t)$ is the cosmic ray density at position $\vec{r}$ at time t for a particle with momentum p, $Q(\vec{r}, p, t)$ is the source term (representing the cosmic ray sources and including production by spallation and decay), $\mathbb{D}_{xx}$ is the spatial diffusion tensor, $\vec{V}$ is the convection velocity, D_{pp} is the diffusion coefficient in momentum space (representing diffusive reacceleration), τ_f is the timescale for loss by fragmentation and τ_d is the timescale for radioactive decay.

The cosmic ray transport equation introduced above can be solved by starting with the solution for the heaviest primary (since it can only be produced at the source, and not via spallation or decay) and using this solution to compute the solutions for the lighter primaries in an iterative way. Because of the complexity,

this can best be done numerically, such as is done in the GALPROP code [Moskalenko et al., 2011].

Considering the fate of the cosmic rays, several things can happen. It is generally believed that they eventually disappear; either by diffusing to the edge of the Galaxy where they then have a finite chance to leak out into intergalactic space, or by means of convection. It is also possible however, that they lose all their energy by inelastic collisions with the interstellar matter. And of course, some of the cosmic rays end up in the atmosphere of the Earth, where they interact and can be observed.

Convection is the movement of particles in a gas or fluid due to differences in density, for instance the rising of warmer air.

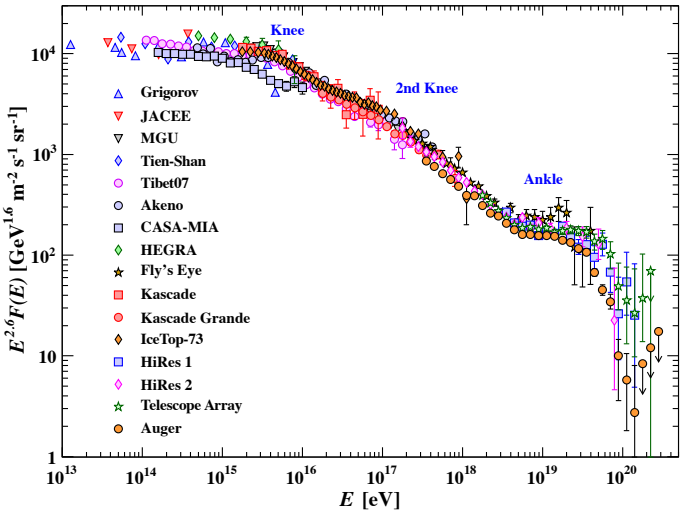

Figure 2.8: All-particle spectrum of cosmic rays as a function of energy-per-nucleus. Figure reproduced from Beringer et al. [2012].

Local cosmic ray flux

As noted before, the cosmic ray flux that is measured at the Earth exhibits a power-law behaviour in its energy spectrum:

$$\Phi_{\mathrm{CR}} \propto E^{-\gamma}, \tag{2.20}$$

where γ is the so-called spectral index. Below an energy of about $5 \cdot 10^6$ GeV it has a value of about 2.7. Above this energy, the spectrum steepens and the spectral index changes to about 3.0. This transition, called the knee, is thought to be due to cosmic ray sources not accelerating protons to beyond this energy and an increase in the escape probability of particles from the Galaxy [Beringer et al., 2012]. At an energy of about $5 \cdot 10^8$ GeV

the spectrum steepens once more ($\gamma \approx 3.3$), a feature which is called the 2nd knee, for which there is no explanation yet. The spectrum hardens again at an energy of about $5 \cdot 10^9$ GeV, a feature called the ankle, and the spectral index changes to about 2.7 again. The ankle is explained either by an extragalactic flux component or by energy losses from cosmic rays interacting with the cosmic microwave background radiation. The different parts of the spectrum can be seen in figure 2.8.

2.2 THEORETICAL MODELS FOR THE NEUTRINO FLUX

Now that the ingredients for the calculation of the diffuse Galactic neutrino flux have been introduced, three theoretical models considered in this work will be discussed. Some assumptions are used in the models to solve the equations analytically. Other approaches exist, such as using GALPROP to solve the cosmic ray transport equation numerically, which is descibed by Jouvenot [2005].

The focus of this work is to perform a measurement of the diffuse Galactic neutrino flux with ANTARES and to determine the sensitivity of KM3NeT. For this goal the theoretical models used here are suitable, since they incorporate the main ingredients. By considering different models, the influence of the assumptions can be checked. Besides using a pure theoretical modelling, experimental observations of high energy γ-rays are used to determine the neutrino fluxes. This will be described in section 2.3.

The names of the models and the references to the papers from which they are obtained are given in table 2.1. The reason for the names of the models will become clear after discussing the assumptions that are made in each of them.

MODEL NAME	REFERENCE
NoDrift_simple	Ingelman and Thunman [1996]
NoDrift_advanced	Candia and Roulet [2003]
Drift	Candia [2005]

Table 2.1: References for the three theoretical models.

2.2.1 *Assumptions*

As input for the determination of the neutrino fluxes, two distributions are needed. These are the matter density and the cosmic ray density as a function of location in the Galaxy. Using cylindrical symmetry, a point in the Galaxy can be identified using two coordinates: the height above/below the Galactic plane z (with $z > 0$ above the Galactic plane) and the distance from the Galactic centre r (in the plane where $z = 0$). The coordinate system is shown in figure 2.9.

Matter distribution

In the two NoDrift models it is assumed that the matter density is constant and has a value of $1\,\text{nucleon/cm}^3$ in the Galactic plane, which has a radius R of 12 kpc. Out of the plane the matter density falls off exponentially, so that it can be parameterised as:

$$\rho_{\text{ISM}}(r, z) = \rho_0 \cdot e^{-|z|/(0.26\,\text{kpc})}, \tag{2.21}$$

with $\rho_0 = 1\,\text{nucleon/cm}^3$.

For the Drift model, a more realistic matter distribution is used which takes into account the higher matter density around the Galactic centre. The radial distribution is taken from the paper from Berezinsky et al. [1993], where it is given in tabular form. The radius of the Galaxy R is taken to be 20 kpc for this model. To avoid steps and ensure a smooth distribution, a function has been fitted to the tabulated values:

$$n(r) = 18.8\,\text{nucleon/cm}^3\ \ (1 - \text{erf}(15.4r\,[\text{kpc}] - 3.5)) + 2.3e^{-0.166r\,[\text{kpc}]}, \tag{2.22}$$

which provides for an accurate parameterisation, see Visser [2013].

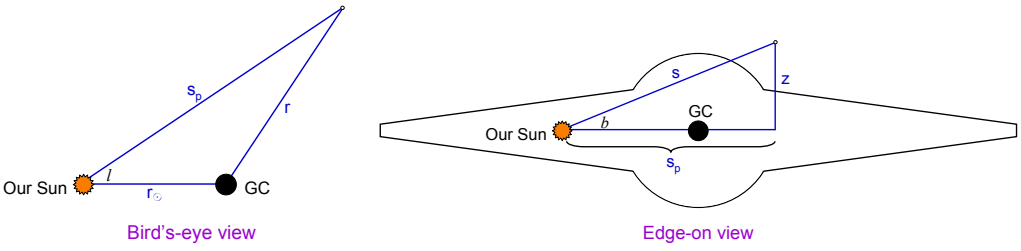

Figure 2.9: Coordinate system used to represent a point in the Galaxy, see the text for details.

Also a different exponential scale height is used[3], so that the matter density as a function of location in the Galaxy becomes:

$$\rho_{\mathrm{ISM}}(r, z) = n(r) \cdot e^{-|z|/(0.5\,\mathrm{kpc})}, \tag{2.23}$$

with $n(r)$ given by equation 2.22. The matter density as seen from outside the Galaxy (in a slice through the Galactic centre) is shown in figure 2.10 (where $r = |x|$).

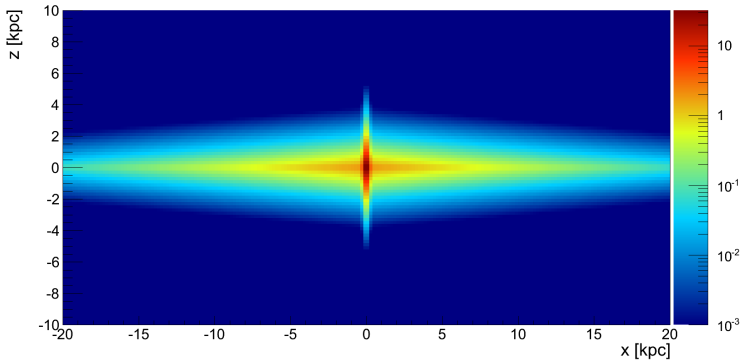

Figure 2.10: Matter density in the Galaxy in nucleon/cm^3 as used in the Drift model.

A useful (and in astronomy often used) quantity is the column density, which is the mass substance (or number of particles) per unit of area as seen from the Earth, integrated along a straight path. For this the Galactic coordinate system is used, where the direction to an object in the sky is expressed in terms of its Galactic longitude l and Galactic latitude b (see also figure 2.9). In this coordinate system, the direction with $l = 0°$ and $b = 0°$ marks the location of the Galactic centre[4]. The column density N is a function of l and b and is given by:

$$N(l, b) = \int \mathrm{d}s\, \rho_{\mathrm{ISM}}(r, z), \tag{2.24}$$

where s is the integration variable (with $s = 0$ at the location of the Earth). Using some geometry, the coordinates used earlier (r and z) can be written in these new coordinates as (see figure 2.9):

$$r(l, b, s) = \sqrt{s^2 \cos^2 b + r_\odot^2 - 2 r_\odot s \cos b \cos l}, \tag{2.25}$$

and:

$$z(l, b, s) = s \sin b, \tag{2.26}$$

[3] *The exponential scale height used by Candia [2005] is not the same as that given in the paper from which the matter distribution is taken [Berezinsky et al., 1993], in which the exponential scale height is ~0.21 kpc for $r < 8$ kpc and ~0.26 kpc for larger values of r. Even though the value of 0.5 kpc is a bit higher than generally assumed (see section 2.1.2), it is compatible with measurements, and the model is used as given by Candia [2005].*

[4] *Actually, the radio source Sagittarius A*, which is the best physical marker of the Galactic centre, is located at $l = 359.94°$ and $b = -0.046°$.*

where $r_\odot$ is the distance from the Earth to the Galactic centre (taken to be 8.5 kpc).

A typical value of the column density is $1\,\mathrm{kpc} \cdot 1\,\mathrm{nucleon/cm^3} \approx 0.3 \cdot 10^{22}\,\mathrm{nucleon/cm^2}$. A plot of the column density for the matter density used in the NoDrift models can be found in figure 2.11 and for the one used in the Drift model in figure 2.12.

Cosmic ray flux

For the NoDrift models, the cosmic ray flux is assumed to be constant throughout the Galaxy and equal to the flux measured locally on Earth. No cosmic ray transport equation is solved and no particle propagation is done, hence the name 'NoDrift', since no drift of cosmic ray particles is considered.

In the NoDrift_simple model the cosmic ray flux is parameterised as:

$$\Phi_\mathrm{N}(E_\mathrm{N}) = \begin{cases} 1.7 \cdot 10^4\, E_\mathrm{N}^{-2.7}\,\mathrm{GeV^{-1}\,m^{-2}\,sr^{-1}\,s^{-1}} & E_\mathrm{N} < 5 \cdot 10^6\,\mathrm{GeV} \\ 174 \cdot 10^4\, E_\mathrm{N}^{-3}\,\mathrm{GeV^{-1}\,m^{-2}\,sr^{-1}\,s^{-1}} & E_\mathrm{N} \geqslant 5 \cdot 10^6\,\mathrm{GeV} \end{cases} \tag{2.27}$$

where Φ_N is the cosmic ray nucleon flux as a function of the nucleon energy E_N and the break represents the knee in the cosmic ray spectrum.

In the NoDrift_advanced model, each nuclear component in the cosmic ray spectrum is modelled separately and the following parameterisation is used for the cosmic ray flux Φ_CR:

$$\Phi_\mathrm{CR}(E) = \sum_Z \frac{\Phi_Z^< \cdot \Phi_Z^>}{\Phi_Z^< + \Phi_Z^>}, \tag{2.28}$$

where $\Phi_Z^<$ ($\Phi_Z^>$) is the CR flux for the component with charge Z and energy E below (above) the knee, which is given by:

$$\begin{Bmatrix} \Phi_Z^< \\ \Phi_Z^> \end{Bmatrix} = f_Z\,\Phi_0 \left(\frac{E}{E_0}\right)^{-\alpha_Z} \cdot \begin{Bmatrix} 1 \\ \left(\frac{E}{ZE_k}\right)^{-2/3} \end{Bmatrix}, \tag{2.29}$$

where $\Phi_0 = 3.5 \cdot 10^{-4}\,\mathrm{GeV^{-1}\,m^{-2}\,sr^{-1}\,s^{-1}}$ is the total CR flux at an energy of $E_0 = 1\,\mathrm{TeV}$, E_k is a parameter fixing the position of the knee, which is taken to be $3.1 \cdot 10^6\,\mathrm{GeV}$ and f_Z and α_Z are the CR fractions and spectral indices per nuclear component for

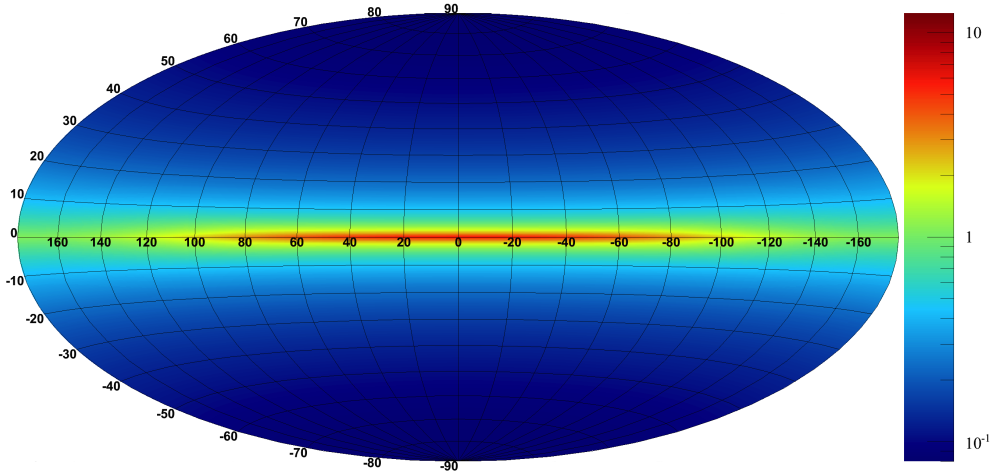

Figure 2.11: Column density in units of 10^{22} nucleon/cm^2 used in the NoDrift models.

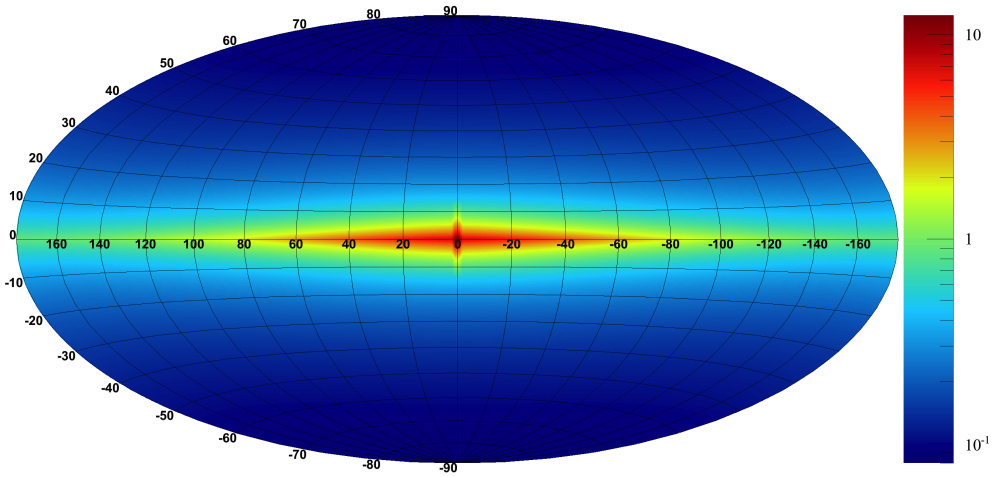

Figure 2.12: Column density in units of 10^{22} nucleon/cm^2 used in the Drift model.

cosmic rays with an energy E_0 respectively. The values of f_Z and α_Z can be found in the paper from Candia and Roulet [2003] and are not repeated here.

In addition to the Galactic component, there is also an extragalactic component, which is assumed to consist only of protons and to permeate the Milky Way homogeneously:

$$\Phi_{XG}(E) = 0.68\, E^{-2.4}\,\mathrm{GeV}^{-1}\,\mathrm{m}^{-2}\,\mathrm{sr}^{-1}\,\mathrm{s}^{-1}, \tag{2.30}$$

with E in GeV.

The cosmic ray flux given by equation 2.28 is the CR particle flux, but for the calculation of the neutrino fluxes, the CR nucleon flux is needed. The particle flux can be converted to a nucleon flux using the following equation[5]:

[5] *Note that the energy in the particle flux is the energy per nucleus, while the energy in the nucleon flux is the energy per nucleon.*

$$\Phi_N(E_N) = \sum_Z A^2\, \Phi_Z(A \cdot E_N), \tag{2.31}$$

where $\Phi_Z(E)$ is the CR particle flux for a single component and A is the average mass number of the element with atomic number Z.

The total cosmic ray nucleon flux can thus be obtained by substituting equation 2.31 in equation 2.28 and adding the extragalactic component from equation 2.30. Since this involves more steps (and assumptions), this model is called the 'NoDrift_advanced' model, while the other NoDrift model is called 'NoDrift_simple'. Since the cosmic ray flux is constant over the Milky Way, the neutrino flux for the NoDrift models will be directly proportional to the column density shown in figure 2.11.

The Drift model is the most advanced model considered here. In it, the cosmic ray transport equation is solved. The steady-state solution is required, so all the time dependence drops out of equation 2.19, which, when also neglecting convection, reacceleration, energy-loss processes and spallation, can be written as:

$$Q(r, z, E) = \vec{\nabla} \cdot \left(\mathbb{D}_{xx} \vec{\nabla} \Phi \right), \tag{2.32}$$

with $Q(r, z, E)$ the source term. This model is also called the *plain-diffusion* model and is generally considered a good description of cosmic ray transport through the Galaxy (at least for energies up to $10^8 \cdot Z$ GeV) [Ptuskin, 2012].

The sources of cosmic rays are assumed to be SNRs, which are distributed within a thin disk with a height h_s, with a radial profile given by:

$$q(r) = \begin{cases} \left(\frac{r}{r_\odot}\right)^{1.69} e^{-3.33\cdot(r-r_\odot)/r_\odot} & r \geqslant 3\,\mathrm{kpc} \\ q(r = 3\,\mathrm{kpc}) & 0\,\mathrm{kpc} < r < 3\,\mathrm{kpc} \end{cases} \tag{2.33}$$

with the part for $r \geqslant 3\,\mathrm{kpc}$ corresponding to the Type II SNR distribution shown as the black line in figure 2.6.

The source term in equation 2.32 can then be written as:

$$Q(r, z, E) = 2h_s q(r)\delta(z)E^{-\beta}, \tag{2.34}$$

where β is the spectral index of the source energy spectrum. In this, it is assumed that the sources lie in a thin disk so that the delta function approximation can be applied.

Concerning the magnetic field, it is assumed that only an azimuthal component with opposite directions above and below the Galactic plane exists (i. e. an anti-symmetric field). The spatial diffusion tensor $\mathbb{D}_{xx}$ can then be written as:

$$\mathbb{D}_{xx} = \begin{pmatrix} D_\perp & 0 & D_A\,\mathrm{sgn}(z) \\ 0 & D_{||} & 0 \\ -D_A\,\mathrm{sgn}(z) & 0 & D_\perp \end{pmatrix}. \tag{2.35}$$

The coefficients $D_{||}$, $D_\perp$ and D_A in equation 2.35 are the diffusion coefficients describing diffusion parallel to the magnetic field lines, diffusion transverse to the magnetic field lines and collective macroscopic diffusion (drift) respectively. The parallel and transverse diffusion coefficients depend on the magnetic field energy density and are assumed to be proportional to $E^{1/3}$, whereas the macroscopic diffusion is proportional to E. This stronger energy dependence of D_A is used by Candia [2005] to explain the knee and the second knee in the cosmic ray energy spectrum as a transition from the transverse diffusion dominated regime to the drift dominated regime.

The drift velocities in the radial and vertical direction can be written as:

$$v_r = -\frac{\partial(D_A\,\mathrm{sgn}(z))}{\partial z} = -2D_A\delta(z), \tag{2.36}$$

$$v_z = \frac{1}{r}\frac{\partial(rD_A\,\mathrm{sgn}(z))}{\partial r} = \frac{2D_A}{r}\mathrm{sgn}(z), \tag{2.37}$$

where the simplifying assumption $D_A(r, z) = D_{A0} \cdot r$ and the relation $\frac{\mathrm{d}(\mathrm{sgn}(z))}{\mathrm{d}z} = 2\delta(z)$ have been used.

The effect of the assumed (anti-symmetric) magnetic field configuration is a radial drift that is directed towards the Galactic centre, as can be seen from equation 2.36. In the case of a symmetric magnetic field there is no radial drift. From equation 2.37 it can be seen that the drift in the vertical direction is removing the CRs from the Galactic plane.

The solution to equation 2.32 (for a single nuclear component), which is set to be unity at $r = r_\odot$ and which is flat at low E is given by[6]:

[6] *For a more detailed derivation of the solution to equation 2.32, see Visser [2013] and Candia [2005].*

$$\Psi(E, r, z) = E^{-2/3} \frac{1 - e^{-w(1-|z|/H)}}{1 - e^{-w}} \int_1^{R/r} \mathrm{d}y \, q(yr) \, y^{-1-2/(e^w-1)}, \tag{2.38}$$

where $H = 2\,\mathrm{kpc}$ is the height of the Galactic disk in which the cosmic ray transport takes place, y is the integration variable which goes from 1 to R/r and

$$w = 0.85 \left(\frac{E}{3 \cdot 10^6\,\mathrm{GeV}} \right)^{2/3}. \tag{2.39}$$

The analytical solution to equation 2.38 can be found in Visser [2013].

Analogously to equation 2.28, the contributions of the separate nuclear components have to be added, so that the total cosmic ray particle flux for the Drift model can be written as:

$$\Phi_{\mathrm{CR}}(E, r, z) = \Phi_0 \sum_Z f_Z \left(\frac{E}{E_0} \right)^{-\alpha_Z} \Psi(E/Z, r, z), \tag{2.40}$$

where Φ_0, E_0, f_Z and α_Z are the same as in equation 2.29.

Like for the NoDrift_advanced model, an extragalactic cosmic ray component is also considered, which is in this case given by:

$$\Phi_{\mathrm{XG}}(E) = 1.3\, E^{-2.4}\,\mathrm{GeV}^{-1}\,\mathrm{m}^{-2}\,\mathrm{sr}^{-1}\,\mathrm{s}^{-1}, \tag{2.41}$$

with E again in GeV. The total cosmic ray nucleon flux can be obtained by adding this result to the Galactic part obtained by applying equation 2.31 on equation 2.40.

The cosmic ray nucleon fluxes for the three models are compared in figure 2.13. It can be seen that the fluxes at the Earth are similar (as they should be, since they have to match the observations), and that the Drift model predicts an increased flux at

MODEL NAME	MATTER DENSITY	R	COSMIC RAY FLUX
NoDrift_simple	Constant (ESH = 0.26 kpc)	12 kpc	Constant
NoDrift_advanced	Constant (ESH = 0.26 kpc)	12 kpc	Constant
Drift	r-dependent (ESH = 0.5 kpc)	20 kpc	Drift of CRs to GC

Table 2.2: Assumptions made by the three theoretical models considered in this work (ESH stands for exponential scale height).

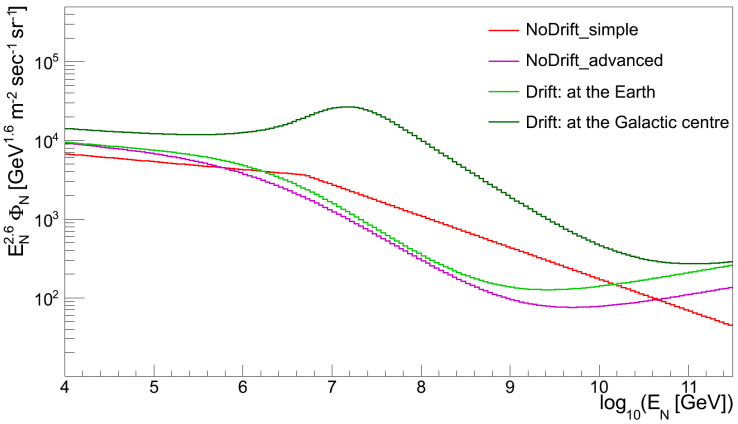

Figure 2.13: Cosmic ray nucleon fluxes predicted by the three theoretical models considered in this work as a function of energy per nucleon.

the Galactic centre. The main difference between the two NoDrift models is the predicted flux at high nucleon energies. This is mainly caused by the fact that no extragalactic component is used in the NoDrift_simple model, so that the ankle in the CR spectrum is not reproduced.

Table 2.2 summarises the assumptions made about the different model components for each of the three models.

2.2.2 *Calculation of $\nu_\mu + \overline{\nu}_\mu$ fluxes*

The matter density and the cosmic ray nucleon fluxes can now be used to calculate the neutrino fluxes. The different processes contributing to neutrino production are described first, after which the neutrino flux calculation is presented. In this, neutrino oscillations are taken into account.

Production mechanisms

Proton-proton interactions can be divided in three different types [Arneodo and Diehl, 2005], see figure 2.14:

A. Non-diffractive (or elastic), in which both protons emerge intact in the final state.

B. Single diffractive, in which one of the protons breaks up and the other one remains intact.

C. Double diffractive, in which both protons break up.

Single and double diffractive interactions are also called inelastic collisions. At the energies considered in this work, a substantial fraction of the total proton-proton cross section is due to inelastic collisions (about 80%, which is then nearly energy independent [Candia, 2005]).

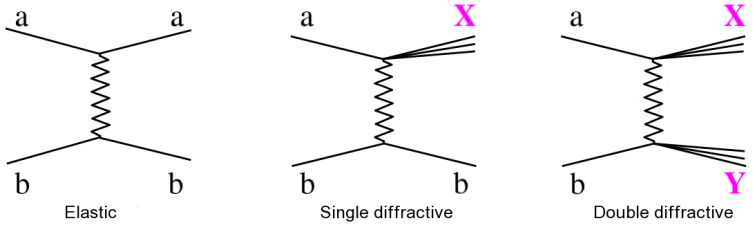

Figure 2.14: The three different types of hadron-hadron interactions. Figure reproduced from Arneodo and Diehl [2005].

Neutrinos are only indirectly produced in inelastic collisions, via the decay of a myriad of leptons and mesons (particles containing a quark and an anti-quark). Since the matter density in the Milky Way is very low, the mesons and leptons that are produced will decay before interacting with another interstellar matter particle. As a result, the maximum energy is transferred to the neutrinos. This sharply contrasts the production of leptons and mesons in cosmic ray interactions in the Earth's atmosphere, see section 2.4.

The main production mechanism is via the decay of charged pions [Huang and Pohl, 2008]:

Pions are the lightest mesons and consist of up and down (anti-)quarks: $\pi^+ = u\bar{d}$, $\pi^- = d\bar{u}$, $\pi^0 = (u\bar{u} - d\bar{d})/\sqrt{2}$.

$$\pi^+ \rightarrow \mu^+ + \nu_\mu, \tag{2.42}$$

and the subsequent decay of the muon:

$$\mu^+ \rightarrow e^+ + \nu_e + \overline{\nu}_\mu, \tag{2.43}$$

where reaction 2.42 happens in about 99.99% of the charged pion decays and reaction 2.43 in almost 100% of the muon decays [Beringer et al., 2012]. The same reactions hold for the anti-particles (by changing particles to anti-particles and vice versa).

Kaons can also decay into neutrinos, where the charged kaon can decay via:

$$\begin{aligned} K^+ &\to \mu^+ + \nu_\mu && (63.55\%) \\ K^+ &\to \pi^0 + e^+ + \nu_e && (5.07\%) \\ K^+ &\to \pi^0 + \mu^+ + \nu_\mu && (3.35\%) \end{aligned} \tag{2.44}$$

and the same again for the K^-. The neutral kaon decays into neutrinos via:

$$\begin{aligned} K^0_L &\to \pi^\pm + e^\mp + \nu_e && (40.55\%) \\ K^0_L &\to \pi^\pm + \mu^\mp + \nu_\mu && (27.04\%) \end{aligned} \tag{2.45}$$

Using the PYTHIA event generator [Sjöstrand et al., 2008] version 8.162, it has been calculated that the contribution of kaon decays to the neutrino production is of the order of 10%, independent of the neutrino energy. The reason that the kaons contribute less than the pions is that the kaon is a factor of about 3.5 heavier than the pion.

The decay of (anti-)neutrons also contributes, but only to the electron-neutrino flux:

$$n \to p + e^- + \overline{\nu}_e, \tag{2.46}$$

which happens in 100% of the decays.

Even heavier mesons, like the charmed mesons $D^\pm$ and D^0, which are important for atmospheric neutrino production (see section 2.4), have a negligible contribution compared to the pion decays [Huang and Pohl, 2008].

So far only muon- and electron-neutrinos[7] have been discussed, since most of the neutrinos that are produced have one of those two flavours[8]. However, tau-neutrinos are also produced, but since lepton number conservation requires a tau-neutrino to be accompanied by a τ-particle (with a mass of $1.78\,\mathrm{GeV}/c^2$), the number of tau-neutrinos is much lower than the number of electron- and muon-neutrinos, see also figure 2.15.

Kaons are the second-lightest mesons and contain a strange (anti-) quark: $K^+ = u\bar{s}$, $K^- = \bar{u}s$, $K^0 = d\bar{s}$, $\overline{K}^0 = \bar{d}s$. The neutral kaons combine into a long-lived and a short-lived state, called K^0_L and K^0_S respectively.

[7] *The subsequent discussions focus on neutrinos, but also hold for anti-neutrinos.*

[8] *Roughly twice as many muon-neutrinos as electron-neutrinos are produced, as can be inferred from reactions 2.42 and 2.43.*

Neutrino yield in proton-proton interactions

The neutrino flux can be calculated from the cosmic ray flux and matter distribution as:

$$\Phi_\nu(E_\nu, l, b) = \int_{E_\nu}^{\infty} \mathrm{d}E_\mathrm{N}\, Y_\nu(E_\mathrm{N}, E_\nu)\, \Phi_\mathrm{T}(E_\mathrm{N}, l, b), \tag{2.47}$$

where $\Phi_\nu(E_\nu, l, b)$ is the neutrino flux (either ν_e, ν_μ or ν_τ) for a given direction, $Y_\nu(E_N, E_\nu)$ is the neutrino yield, i.e. the number of neutrinos produced in the interval E_ν to $E_\nu + \delta E_\nu$ per proton-proton interaction (see Engel [2008] for an overview) and $\Phi_T(E_N, l, b)$ is the cosmic ray nucleon flux times the number of proton-proton interactions per metre, integrated along the line of sight:

$$\Phi_T(E_N, l, b) = \int \mathrm{d}s \; \Phi_N(E_N, r, z)\, \rho_{ISM}(r, z)\, \sigma_{pp}(E_N), \quad (2.48)$$

where $\sigma_{pp}(E_N)$ is the total proton-proton cross section. For the NoDrift models, the cosmic ray flux does not depend on position in the Galaxy, so that the integral along the line of sight in equation 2.48 reduces to the product of the cosmic ray nucleon flux, the total cross section and the column density (equation 2.24).

The neutrino yield is calculated by simulating fixed target proton-proton collisions with the PYTHIA event generator. It is important to point out that only proton-proton interactions are simulated; however the interstellar medium also consists of a small fraction of helium (having two neutrons in addition to two protons) and cosmic rays also contain particles with neutrons. Since PYTHIA cannot simulate these neutron-proton and neutron-neutron interactions, they are not included. However, at the energies of interest, the interactions that take place are mainly gluon-gluon interactions and the neutron and proton can be considered identical. The error arising from only simulating proton-proton interactions is thus small, see also Kamae et al. [2005].

The interactions are simulated in the Centre Of Momentum (COM) frame and the result is then Lorentz boosted to the universal frame. It is important to force the pions and muons to decay in order to produce neutrinos, since they are normally considered stable for collider experiments.

The muon-neutrino yield is shown in the top left plot of figure 2.15; the result for anti-muon-neutrinos is similar. It can be seen that in order to produce a neutrino with an energy of for instance 10 TeV, nucleons with an energy of at least 10 TeV are needed, as expected. Cosmic ray nucleons with an energy of $E_N \approx 10 \cdot E_\nu$ contribute the most to the neutrino flux at an energy of E_ν [Kachelrieß and Ostapchenko, 2014]. This results from the interplay of the neutrino yield, which rises with cosmic ray energy, the proton-proton cross section, which also rises with energy and the cosmic ray flux, which falls off as $E^{-2.7}$.

The electron- and tau-neutrino yields are shown in the top right and bottom plot of figure 2.15 respectively. The electron-neutrino

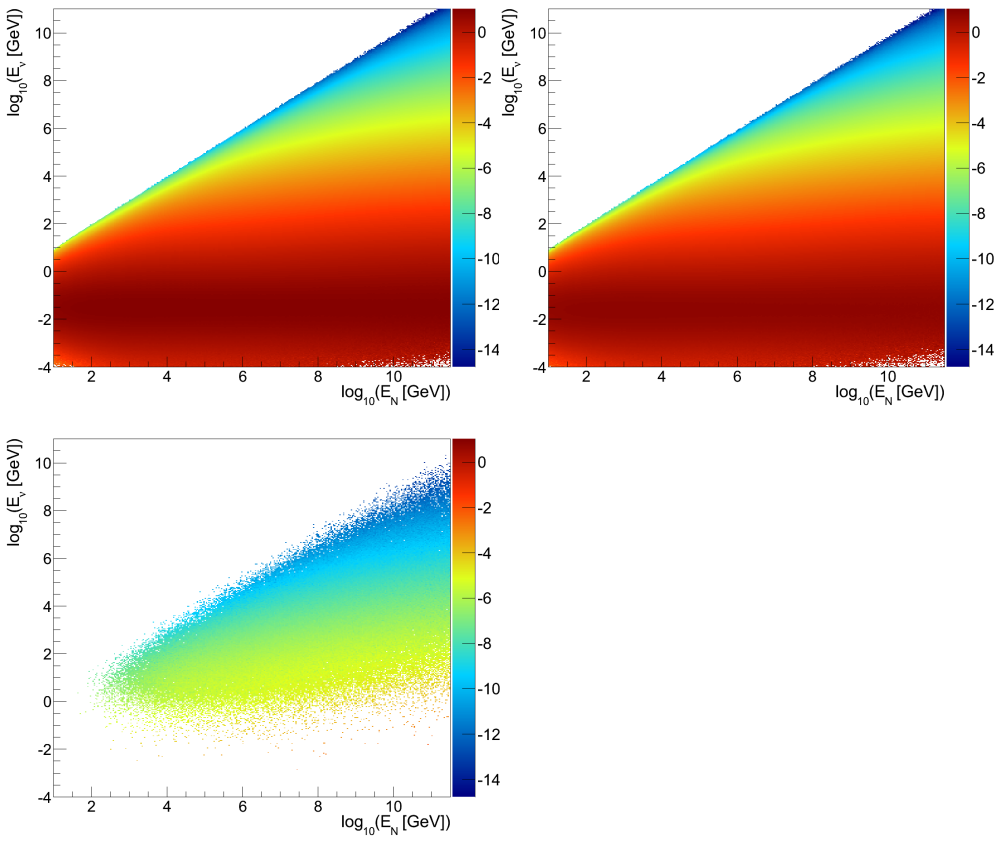

Figure 2.15: Logarithm of the neutrino yield in units of GeV^{-1} versus energy of the incoming proton and neutrino energy. TOP LEFT: for muon-neutrinos. TOP RIGHT: for electron-neutrinos. BOTTOM LEFT: for tau-neutrinos.

yield is similar to the muon neutrino yield, just about a factor of 2 lower. The tau-neutrino yield is much lower than the electron- and muon-neutrino yield, as expected.

Neutrino oscillations

In the late 1960s the Homestake Experiment used to observe solar neutrinos to study the nuclear fusion reactions in the Sun. However, the detector recorded less electron-neutrinos than theoretically predicted, leading to the so-called *solar neutrino problem* [Grupen, 2005]. With the SNO detector, which was sensitive to all three neutrino flavours, one could observe that the total neutrino flux from the Sun (i. e. including muon- and tau-neutrinos)

SNO: Sudbury Neutrino Observatory

was in accordance with theoretical predictions, but that electron-neutrinos disappeared. The solar neutrino problem was solved! The explanation is that the electron-neutrinos oscillate into muon- and tau-neutrinos on their way to the Earth.

Neutrino oscillations imply that neutrinos are not massless, as was previously assumed, but that at least two of the neutrino flavours have a mass. Oscillations occur when the flavour eigenstates are not the same as mass eigenstates, but a linear superposition of them, e. g.:

$$\begin{pmatrix} \nu_e \\ \nu_\mu \\ \nu_\tau \end{pmatrix} = \begin{pmatrix} c_{12}c_{13} & s_{12}c_{13} & s_{13}e^{-i\delta} \\ -s_{12}c_{23} - c_{12}s_{13}s_{23}e^{i\delta} & c_{12}c_{23} - s_{12}s_{13}s_{23}e^{i\delta} & c_{13}s_{23} \\ s_{12}s_{23} - c_{12}s_{13}c_{23}e^{i\delta} & -c_{12}s_{23} - s_{12}s_{13}c_{23}e^{i\delta} & c_{13}c_{23} \end{pmatrix} \begin{pmatrix} \nu_1 \\ \nu_2 \\ \nu_3 \end{pmatrix}, \tag{2.49}$$

where the abbreviations $s_{ij} \equiv \sin\theta_{ij}$ and $c_{ij} \equiv \cos\theta_{ij}$ are used, and where ν_i are the mass eigenstates, ν_α are the flavour eigenstates, θ_{ij} are the mixing angles and δ is the complex phase, which allows for CP violation in the neutrino sector [Martin and Shaw, 2008].

The oscillation of a neutrino of flavour α to flavour β (which can be the same as α) is given by [Anchordoqui et al., 2014]:

$$P_{\nu_\alpha \to \nu_\beta} = \delta_{\alpha\beta} - 4\sum_{i>j} \Re(U^*_{\alpha i} U_{\beta i} U_{\alpha j} U^*_{\beta j}) \sin^2 \Delta_{ij} + 2\sum_{i>j} \Im(U^*_{\alpha i} U_{\beta i} U_{\alpha j} U^*_{\beta j}) \sin(2\Delta_{ij}), \tag{2.50}$$

where $U_{\alpha i}$ etc. denote elements from the matrix as given in equation 2.49 and the oscillation phase Δ_{ij} is given by:

$$\Delta_{ij} = \frac{\Delta m^2_{ij} L}{4E_\nu} \approx 1.27 \frac{\Delta m^2_{ij}\,[\mathrm{eV}^2] L\,[\mathrm{km}]}{E_\nu\,[\mathrm{GeV}]}, \tag{2.51}$$

where $\Delta m^2_{ij} \equiv m^2_i - m^2_j$ is the mass squared difference between mass eigenstates and L is the distance the neutrino has travelled.

With the recent measurement of θ_{13} by the Daya Bay experiment, the values of all three mixing angles are now known [Weiler, 2013]: $\theta_{12} \simeq 35°$, $\theta_{23} \simeq 43°$ and $\theta_{13} \simeq 9°$. Nothing is known yet about the complex phase δ.

A good approximation is to adopt maximal mixing for $\nu_\mu \leftrightarrow \nu_\tau$ (so $\theta_{23} = 45°$) and neglect terms with θ_{13} [Anchordoqui et al., 2014]. Furthermore, since the focus is here on neutrinos travelling from anywhere in the Milky Way to Earth, L is large and

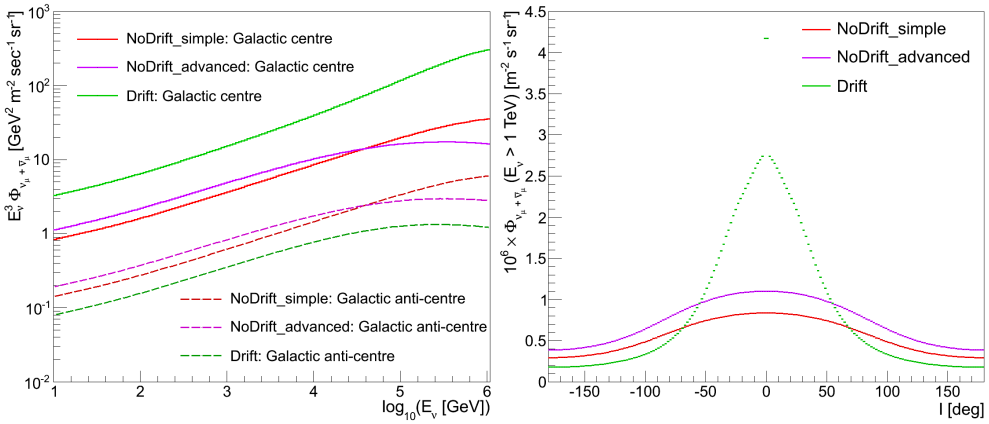

Figure 2.16: Neutrino fluxes for the three theoretical models. LEFT: versus neutrino energy. RIGHT: versus Galactic longitude.

varies for each neutrino, so that $\sin^2 \Delta_{ij}$ can be averaged over and equation 2.50 can be written as:

$$P_{\nu_\alpha \to \nu_\beta} = \sum_i U_{\alpha i} U_{\beta i}, \tag{2.52}$$

or in matrix form as[9]:

$$\begin{pmatrix} \hat{\nu}_e \\ \hat{\nu}_\mu \\ \hat{\nu}_\tau \end{pmatrix} = \begin{pmatrix} 1 - \frac{1}{2}\sin^2 2\theta_{12} & \frac{1}{4}\sin^2 2\theta_{12} & \frac{1}{4}\sin^2 2\theta_{12} \\ \frac{1}{4}\sin^2 2\theta_{12} & \frac{1}{2} - \frac{1}{8}\sin^2 2\theta_{12} & \frac{1}{2} - \frac{1}{8}\sin^2 2\theta_{12} \\ \frac{1}{4}\sin^2 2\theta_{12} & \frac{1}{2} - \frac{1}{8}\sin^2 2\theta_{12} & \frac{1}{2} - \frac{1}{8}\sin^2 2\theta_{12} \end{pmatrix} \begin{pmatrix} \nu_e \\ \nu_\mu \\ \nu_\tau \end{pmatrix}, \tag{2.53}$$

where $\hat{\nu}_\alpha$ represent the flavour eigenstates after oscillation. The same equation holds for anti-neutrinos.

[9] *A useful trigonometric identity is* $cos^4 x + sin^4 x = 1 - \frac{1}{2} sin^2 2x$.

Neutrino fluxes

The neutrino fluxes obtained for the three theoretical models including oscillations are compared in figure 2.16. These and all following plots show the sum of muon-neutrino and anti-neutrino fluxes, unless stated otherwise. The electron- and tau-neutrino fluxes are not shown, since these neutrinos are not used in the analysis, due to the signatures they leave in the detector, see chapter 3.

The left plot in figure 2.16 shows the fluxes versus energy for two directions, whereas the right plot shows the fluxes versus Galactic longitude, averaged over Galactic latitude ($|b| < 4.5°$) and integrated above a neutrino energy of 1 TeV.

It can be seen that the fluxes for the different models agree with each other to within a factor of about 3. The models consistently show that the flux peaks in the direction of the Galactic centre. The Drift model predicts a higher flux around the Galactic centre than the NoDrift models, and a lower flux near the Galactic anti-centre ($l = 180°$). This is caused by the drift of cosmic rays from the outer parts of the Milky Way towards the GC.

The three theoretical models used here only constitute a small subset of all possible models, and other assumptions can be made that would result in slightly different predictions, see for instance the paper by Evoli et al. [2007]. The models used here give a good general idea about the flux. Instead of calculating neutrino fluxes by using more theoretical models, the neutrino flux is also determined in a different way, which will be described in the next section.

2.3 CALCULATION OF NEUTRINO FLUXES FROM FERMI γ-RAY FLUX

To get an independent estimate for the neutrino flux, the γ-ray flux measured by the Fermi satellite is used and converted into a neutrino flux. It is widely accepted that part of the γ-ray flux is of hadronic origin, i. e. comes from π^0-decays (see below), at least for the emission from the Galactic plane (see also the paper by Kamae et al. [2005] and the references therein). The main assumption made in this method of estimating the neutrino flux, is the fraction of the γ-ray flux coming from π^0-decays.

The MILAGRO (meaning miracle in Spanish) experiment was a ground based water Čerenkov telescope.

A similar procedure has been applied in the paper by Taylor et al. [2009], in which the γ-ray data measured by MILAGRO in combination with EGRET data are used. The procedure applied in this paper uses some simplifying assumptions. It is assumed that all photons are of hadronic origin and the flux in the inner Galaxy ($-40° < l < 40°$ and $-2° < b < 2°$) is obtained by scaling the MILAGRO results (which only measures the part of the inner Galaxy between a longitude of 30° and 40°) with the help of the EGRET results.

EGRET: Energetic Gamma Ray Experiment Telescope: one of the experiments aboard the Compton Gamma Ray Observatory (CGRO) satellite.

Here instead, the Fermi data are used, which cover the full sky with much higher statistics and show a good angular resolution (see below). Although the data do not extend to energies of 10 TeV like the MILAGRO data, it extends far enough in energy (~600 GeV) to give a reliable estimate of the expected neutrino fluxes.

2.3.1 *Photon flux measured by Fermi*

The LAT instrument aboard the Fermi satellite detects photons, with energies that range from about 20 MeV to over 300 GeV, by recording the electron-positron pairs created by individual γ-rays [Ackermann et al., 2012c]. Since the focus of this thesis is on the diffuse Galactic neutrino flux, point sources of photons are not important, and it is the diffuse γ-ray flux as measured by the Fermi collaboration that is used. The Fermi collaboration provides these data on their website[10] in the form of a .fits file (`gal_2yearp7v6_v0.fits`), in which they have subtracted the fluxes of all known point sources. The diffuse photon sky-map at an energy of 3.4 GeV is shown in Galactic coordinates in figure 2.17. This figure is similar to the bottom right plot of figure 1.3, except for the fact that the point sources of γ-rays have been subtracted.

[10] *See* `fermi.gsfc.nasa.gov/ssc/data/access/lat/BackgroundModels.html`

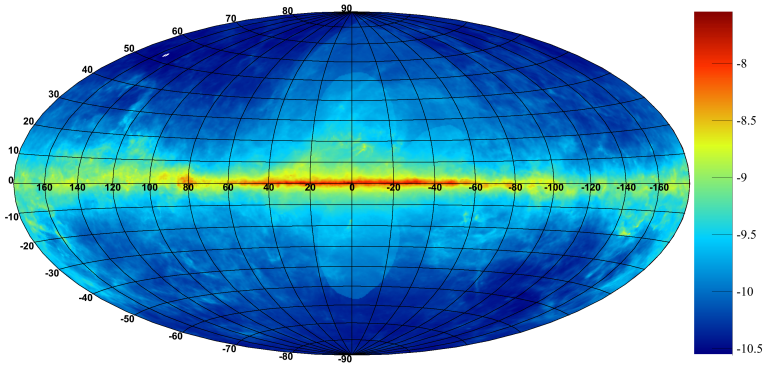

Figure 2.17: Sky-map of the diffuse γ-ray flux in units of $\mathrm{GeV}^{-1}\,\mathrm{m}^{-2}\,\mathrm{sr}^{-1}\,\mathrm{s}^{-1}$ at an energy of 3.4 GeV.

The Fermi diffuse flux is binned in 30 bins in energy (going from 50 MeV to 600 GeV), and the sky-map contains 2880 pixels in Galactic longitude and 1441 in Galactic latitude. Only the last 17 of the energy bins (from 3.4 GeV to 600 GeV) will be used. A simple single power law describes well the data above 3.4 GeV. The photon flux for each of the pixels is parameterised as:

$$\Phi_\gamma(E_\gamma) = A\,E_\gamma^{-B}, \tag{2.54}$$

where Φ_γ is the photon flux and E_γ is the photon energy. A and B are the flux constant and spectral index respectively, which will be fitted.

In general the fit works very well, as can be seen from the left plot in figure 2.18, which shows a typical γ-ray spectrum

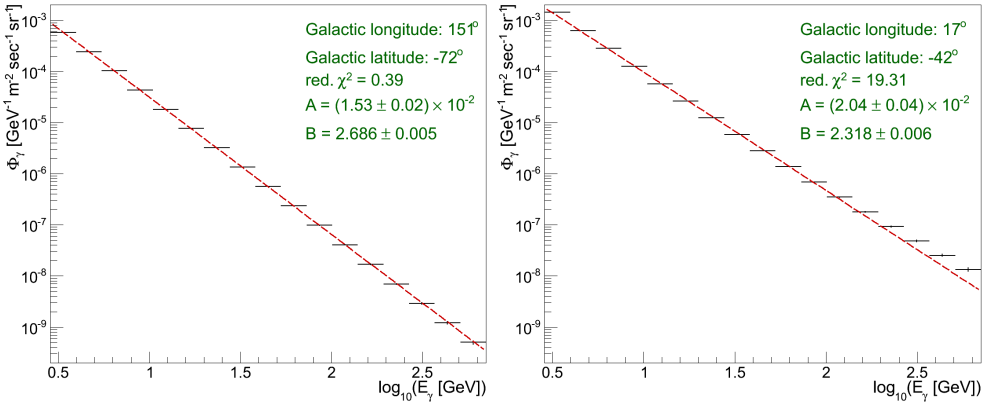

Figure 2.18: The photon flux versus energy, fitted with equation 2.54. LEFT: an example of a good fit. RIGHT: an example of a bad fit.

together with the fit. Sometimes the fit does not work so well (see the right plot in figure 2.18), which can be attributed to the Fermi bubbles. It can be seen from the figure that the distribution cannot be described by a single power law. It appears to consist of two separate contributions, the standard diffuse flux and some contribution becoming dominant at higher energies. It is possible to correct for this and also get an estimate for the flux from the Fermi bubbles in this way, but since this is beyond the scope of this work it has not been pursued and the Fermi bubble region has been omitted altogether.

The reduced χ^2 value of the fit (i. e. the χ^2 divided by the number of degrees of freedom) is typically between 0.3 and 2.0, except for the Fermi bubbles, which can be clearly distinguished in the sky-map of the reduced χ^2 shown in figure 2.19. Also the spectral index (parameter B in equation 2.54) is different for the Fermi bubbles, as can be seen in figure 2.20, which shows a sky-map of the spectral indices obtained in the fit. The spectral index is generally found to be between about 2.6 and 2.7, but is significantly lower for the Fermi bubbles, namely around 2.2. It should be noted though, that the spectral index in the Fermi bubbles is not correct and should be even lower than the one obtained here, see also the right plot in figure 2.18. The spectral index in the inner Galactic plane[11] is found to be slightly lower (between about 2.5 and 2.6) than in the rest of the sky, as also found by Taylor et al. [2009]. This can be seen in figure 2.21, in which the distributions of the fitted spectral indices in the inner Galaxy and the rest of the sky are shown.

[11] *Defined as* $|l| < 40°$ *and* $|b| < 4°$.

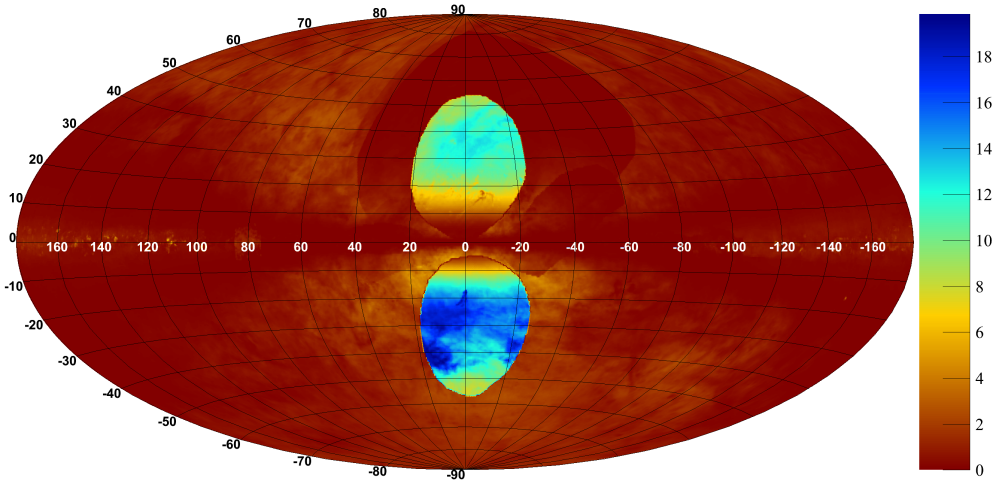

Figure 2.19: Sky-map of the reduced χ^2 value of the fit.

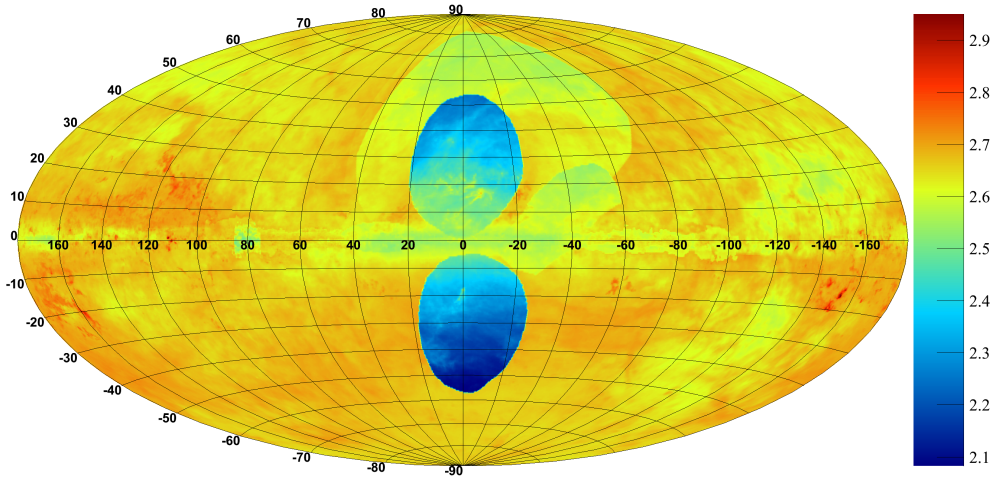

Figure 2.20: Sky-map of the spectral index obtained in the fit.

Lower spectral indices are not only found in the inner Galactic plane, but also in some structure above the upper Fermi bubble and in a structure that starts near $l = 30°$, $b = 10°$ and extends towards smaller longitude and larger latitude values. The first of these structures corresponds to the North Polar Spur associated with Loop I [Su et al., 2010]. There is no explanation for the second structure, but a template has been developed by the Fermi collaboration[12] in order to remove it. However, since the focus lies here on the Galactic plane (with $|b| < 5°$), this correction is not applied here.

[12] *Which can be found at* `fermi.gsfc.nasa.gov/ssc/data/access/lat/Model_details/Pass7_galactic.html`

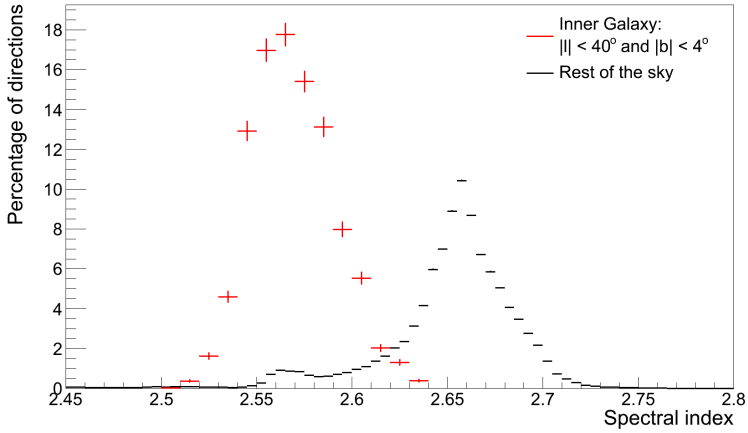

Figure 2.21: Distributions of the spectral index obtained in the fit.

The errors obtained from the fit are of the order of 1.5% for the flux constant and of the order of 0.2% for the spectral index in the cases where the fit worked well (i. e. had a reduced χ^2 around 1) and are not taken into account as part of the systematic error. This is justified since the systematic error from the uncertainty in the effective area of the Fermi-LAT instrument is about a factor of 10 bigger. This error is 14.4% at 3.4 MeV and 20% above 10 GeV, with linear interpolation in logartithm of energy in between [Ackermann et al., 2012b].

2.3.2 *Photon flux from π^0-decays*

Several mechanisms can produce γ-rays, see also figure 2.22:

A. Synchrotron radiation, which occurs when a charged particle is deflected in a magnetic field.

B. Bremsstrahlung, which is similar to synchrotron radiation, but in this case the charged particle is deflected in the Coulomb field of a nucleus instead of in a magnetic field.

C. Inverse Compton (IC) scattering, in which a low energy photon (for instance from the cosmic microwave background) is blueshifted by the collision with an energetic electron.

D. Matter-antimatter annihilation, mostly electron-positron and proton-antiproton annihilations.

E. Decay of subatomic particles, like the π^0 or the η^0, see below.

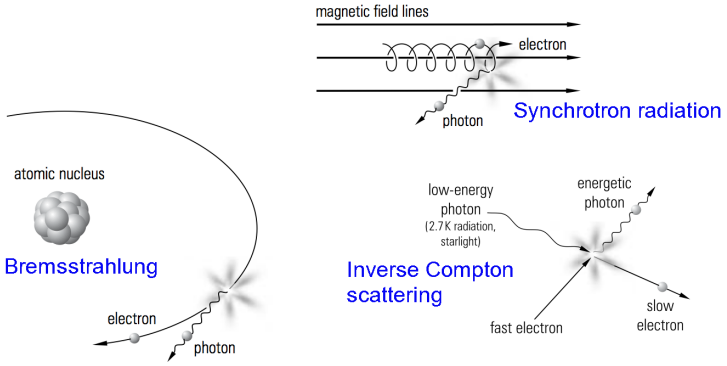

Figure 2.22: Some of the mechanisms that can produce γ-rays. Figure reproduced from Grupen [2005].

Concerning the decay of subatomic particles, almost all of them have one or more decay modes involving photons, but for the current discussion only the neutral pion and the η^0-particle are important, since they are the lightest neutral unflavoured mesons. Photons are produced from these particles via:

The η^0-meson is a combination of up, down and strange (anti-)quarks: $\eta^0 = \frac{u\bar{u} + d\bar{d} - 2s\bar{s}}{\sqrt{6}}$.

$$\begin{aligned} \pi^0 &\rightarrow \gamma + \gamma \qquad (98.82\%) \\ \pi^0 &\rightarrow e^+ + e^- + \gamma \qquad (1.17\%) \end{aligned} \tag{2.55}$$

and:

$$\begin{aligned} \eta^0 &\rightarrow \gamma + \gamma \qquad (39.31\%) \\ \eta^0 &\rightarrow \pi^+ + \pi^- + \gamma \qquad (4.60\%) \end{aligned} \tag{2.56}$$

Both of these mesons are commonly produced in proton-proton interactions and will contribute to the number of observed γ-rays.

However, since about a factor of 10 more π^0 particles than η^0 particles are produced and the η^0 only decays to photons in about 44% of the cases, the contribution from π^0 particles will be the dominant one. Using the PYTHIA event generator, it has been calculated that the contribution of η^0-decays to photon production is of the order of 10%, independent of photon energy. The contribution of η^0-decays is not taken into account, leading to an overestimation of the π^0-flux and thus of the neutrino fluxes of the order of 10%.

Of the mechanisms described above, IC scattering and π^0-decay are the most important at photon energies $\gtrsim 10\,\mathrm{GeV}$, see also figure 2.23. The relative importance of these two processes depends on the density of electrons and photons compared to the density of CRs and interstellar matter. In the Galactic plane, where the density of protons is maximal, the main contribution will thus come from π^0-decays, while at high latitudes the IC scattering contribution is higher.

The contributions of these two processes (and also bremsstrahlung) have been determined by the Fermi collaboration for several regions in Galactic coordinates. The region with $-80^\circ \leqslant l \leqslant 80^\circ$ and $-8^\circ \leqslant b \leqslant 8^\circ$ (referred to as region 1) encompasses the (inner) Galactic plane. This is the region of most interest in this work. Also the region with $80^\circ < l < 280^\circ$ and $-8^\circ \leqslant b \leqslant 8^\circ$ (referred to as region 2) is important, since it encompasses the signal region used by the AMANDA-II experiment. In order to obtain neutrino flux predictions for the whole sky, also the region with $0^\circ \leqslant l < 360^\circ$ and $8^\circ < |b| \leqslant 90^\circ$ is considered.

Several different models are used by the Fermi collaboration to fit the diffuse γ-ray flux, which differ in the CR source distribution, the size of the volume in which the CRs can propagate and the distribution of interstellar matter. The models are constrained to reproduce the locally observed CR fluxes and the predicted γ-ray flux is compared to data using a maximum-likelihood fit. In this fit, the fluxes and spectra of an isotropic γ-ray background component and of known point sources, the strength of the infrared and optical radiation field and a parameter relating to the matter composition can be varied. As an example, figure 2.23 shows the fit results for region 2 for four different models. For more details, see the paper from Ackermann et al. [2012b].

Since neutrinos are produced (mainly) from charged pion decays, the contribution of π^0-decays to the total diffuse γ-ray flux is needed for the determination of the neutrino fluxes. This contribution (which is energy dependent, as can be seen from figure 2.23), together with its uncertainty, is estimated from the models used

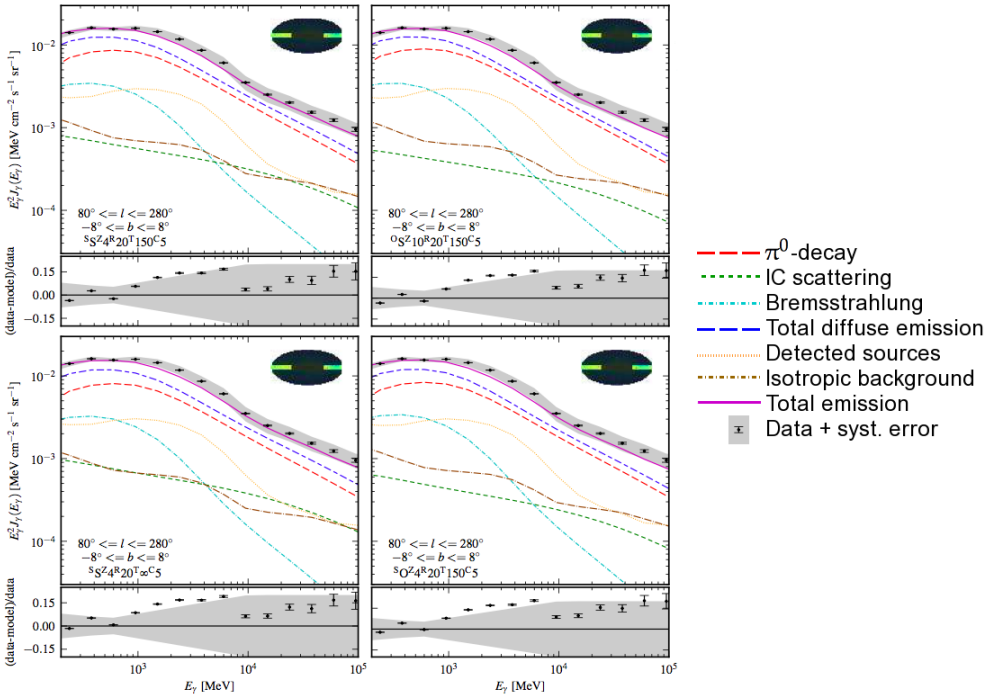

Figure 2.23: Fermi γ-ray data for the region with $80^\circ < l < 280^\circ$ and $-8^\circ \leqslant b \leqslant 8^\circ$ (i. e. region 2), with the contribution from the several components obtained from the fit for four different models. Figure reproduced from Ackermann et al. [2012b].

by the Fermi collaboration. The percentage of all photons originating from neutral pion decays is around 70% for region 2 and is independent of photon energy. For region 1 the percentage varies from about 70% at 10 GeV to an extrapolated 45% at 1 PeV. The difference between the models gives a systematic error of about 15% over the whole energy range.

An important aspect that should be mentioned is the attenuation of photons, since it could lead to a wrong (too low) estimate of the neutrino flux. However, since attenuation only plays a role for photon energies above about 10 TeV for the (Galactic) distances considered here it is not important [Moskalenko et al., 2006].

2.3.3 *Determination of pion fluxes*

By using PYTHIA, the γ-ray flux from π^0-decays can be converted into the π^0-flux, which can in turn be converted into the $\pi^\pm$-fluxes.

The π^0-flux

Analogously to computing the neutrino flux from the cosmic ray flux, the γ-ray flux can be computed from the π^0-flux as:

$$\Phi_\gamma(E_\gamma) = \int_{E_\gamma}^{\infty} \mathrm{d}E_{\pi^0}\, Y_\gamma(E_{\pi^0}, E_\gamma)\, \Phi_{\pi^0}(E_{\pi^0}), \tag{2.57}$$

where $\Phi_{\pi^0}(E_{\pi^0})$ is the neutral pion flux as a function of energy of the neutral pion E_{π^0}. This equation is very similar to equation 2.47, but does not contain a cross section term, since the probability is 100% that the π^0 will decay at some point. It has been assumed that the π^0 does not interact before decaying (which would cause it to lose energy), which is justified since the matter density in the Milky Way is very low and the π^0 decays rapidly.

Equation 2.57 can also be written in matrix-vector form as:

$$\begin{pmatrix} \Phi_\gamma(E_{\gamma,1}) \\ \Phi_\gamma(E_{\gamma,2}) \\ \Phi_\gamma(E_{\gamma,3}) \\ \vdots \end{pmatrix} = \begin{pmatrix} Y_{\gamma,11}\mathrm{dE}_{\pi^0,1} & Y_{\gamma,12}\mathrm{dE}_{\pi^0,2} & \cdots \\ Y_{\gamma,21}\mathrm{dE}_{\pi^0,1} & Y_{\gamma,22}\mathrm{dE}_{\pi^0,2} & \cdots \\ Y_{\gamma,31}\mathrm{dE}_{\pi^0,1} & Y_{\gamma,32}\mathrm{dE}_{\pi^0,2} & \cdots \\ \vdots & \vdots & \ddots \end{pmatrix} \begin{pmatrix} \Phi_{\pi^0}(E_{\pi^0,1}) \\ \Phi_{\pi^0}(E_{\pi^0,2}) \\ \Phi_{\pi^0}(E_{\pi^0,3}) \\ \vdots \end{pmatrix}, \tag{2.58}$$

which can then be inverted to obtain the π^0-flux from the γ-ray flux:

$$\begin{pmatrix} \Phi_{\pi^0}(E_{\pi^0,1}) \\ \Phi_{\pi^0}(E_{\pi^0,2}) \\ \Phi_{\pi^0}(E_{\pi^0,3}) \\ \vdots \end{pmatrix} = \mathbb{Y}_\gamma^{-1} \begin{pmatrix} \Phi_\gamma(E_{\gamma,1}) \\ \Phi_\gamma(E_{\gamma,2}) \\ \Phi_\gamma(E_{\gamma,3}) \\ \vdots \end{pmatrix}, \tag{2.59}$$

where $\mathbb{Y}_\gamma^{-1}$ is the inverse of the matrix in equation 2.58.

To obtain the inverted matrix, PYTHIA is used again. However, instead of simulating proton-proton interactions, PYTHIA is used in the so-called *single-particle gun* mode. In this mode, an unstable particle with a certain energy is given as input, which is then forced to decay.

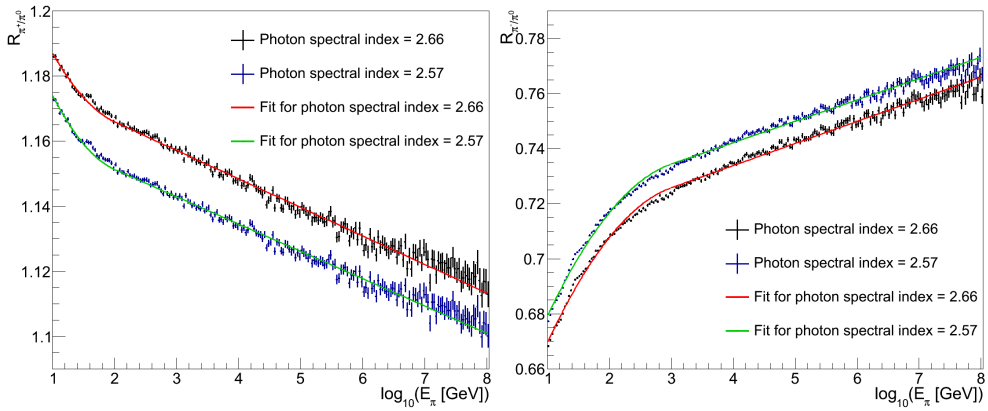

Figure 2.24: Ratios of the charged to neutral pion fluxes versus pion energy. LEFT: R_{π^+/π^0}. RIGHT: R_{π^-/π^0}.

The $\pi^{\pm}$-flux

To obtain the π^+- and π^--fluxes corresponding to a given π^0-flux, proton-proton interactions have been simulated in PYTHIA and the π^+-, π^-- and π^0-fluxes are obtained using the same method as for obtaining the neutrino fluxes:

$$\Phi_\pi(E_\pi) = \int_{E_\pi}^{\infty} \mathrm{d}E_\mathrm{N}\, Y_\pi(E_\mathrm{N}, E_\pi)\, \Phi_\mathrm{N}(E_\mathrm{N})\, \sigma_\mathrm{pp}(E_\mathrm{N}). \quad (2.60)$$

Then, the ratios of the π^+- to the π^0-flux (named R_{π^+/π^0}) and the π^-- to the π^0-flux (named R_{π^-/π^0}) are determined as a function of the pion energy. The $\pi^{\pm}$-fluxes are obtained from the π^0-fluxes by multiplying the latter by the corresponding ratio. This can be done, since the mass of the neutral and charged pions is nearly identical (139.6 MeV/c^2 for the charged pions compared to 135.0 MeV/c^2 for the neutral pion), so that $E_{\pi^+} \approx E_{\pi^-} \approx E_{\pi^0} = E_\pi$.

Two different proton spectra are used (i. e. $\Phi_\mathrm{N}(E_\mathrm{N})$ in equation 2.60), which have been chosen to reproduce a γ-ray flux with a spectral index corresponding to the average spectral index obtained in the fit to the photon flux. A proton spectrum with a spectral index of 2.63 gives a γ-ray spectrum with a spectral index of about 2.56, i. e. reproducing the photon flux in the inner Galaxy. A proton spectrum with a spectral index of 2.72 gives a γ-ray spectrum with a spectral index of about 2.66, i. e. reproducing the photon flux in the rest of the sky (see also figure 2.21).

The ratios R_{π^+/π^0} and R_{π^-/π^0} are shown as a function of pion energy in figure 2.24. It can be seen that these ratios are energy

dependent. The higher the pion energy is, and thus the energy of the proton that created the pion, the closer the ratio to unity. This can be understood from the fact that the higher the COM energy of the interaction is, the more likely it is that a gluon-gluon interaction takes place (as opposed to a gluon-quark or quark-quark interaction), in which it is equally likely to produce a charged or a neutral pion.

The ratios also depend on the spectral index of the proton flux; the higher the spectral index is, the higher R_{π^+/π^0} and the lower R_{π^-/π^0}. This is caused by the fact that a higher spectral index results in a softer energy spectrum[13], so that relatively less gluon-gluon interactions take place and more positively charged pions are created compared to negatively charged pions. The latter comes from the fact that the proton has a positive charge. The shape of the ratio however, is invariant under the variation of the spectral index.

[13] *In a softer energy spectrum there are relatively more low energy events than in a harder spectrum.*

The ratios have been fitted with a parabolic function in the logarithm of the pion energy from 1 to 2 (1 to 3) and with a straight line in the logarithm of the pion energy from 2 to 8 (3 to 8) for R_{π^+/π^0} (R_{π^-/π^0}). By comparing the left and right plots in figure 2.24, it can be seen that the difference in the ratio is only about 1% for the two different spectral indices. The inner Galaxy and the rest of the sky are treated separately, i. e. different ratios are used, but the variation of the spectral index within the region (see figure 2.21) is ignored. This is justified, since the error made in this way is of the order of a tenth of a percent, and can thus be ignored compared to the other sources of systematic error.

2.3.4 *Obtained $\nu_\mu + \overline{\nu}_\mu$ fluxes*

To obtain the neutrino fluxes from the π^+- and π^--fluxes is again straightforward:

$$\Phi_\nu(E_\nu) = \int_{E_\nu}^{\infty} \mathrm{d}E_{\pi^\pm}\; Y_{\nu,\pm}(E_{\pi^\pm}, E_\nu)\, \Phi_{\pi^\pm}(E_{\pi^\pm}), \qquad (2.61)$$

where $Y_{\nu,\pm}(E_{\pi^\pm}, E_\nu)$ is the neutrino yield from $\pi^\pm$-decays. The yields for postively charged and negatively charged pions are determined separately, so to obtain the total neutrino or anti-neutrino flux the contributions have to be added. The yields are again determined using PYTHIA in the *single-particle gun* mode.

For the calculation of the neutrino fluxes, it has been assumed that all neutrinos are created through $\pi^\pm$-decay (and the subsequent μ-decay). However, neutrinos can also be produced via $K^\pm$- or K^0_L-decays, see reactions 2.44 and 2.45. This contribution

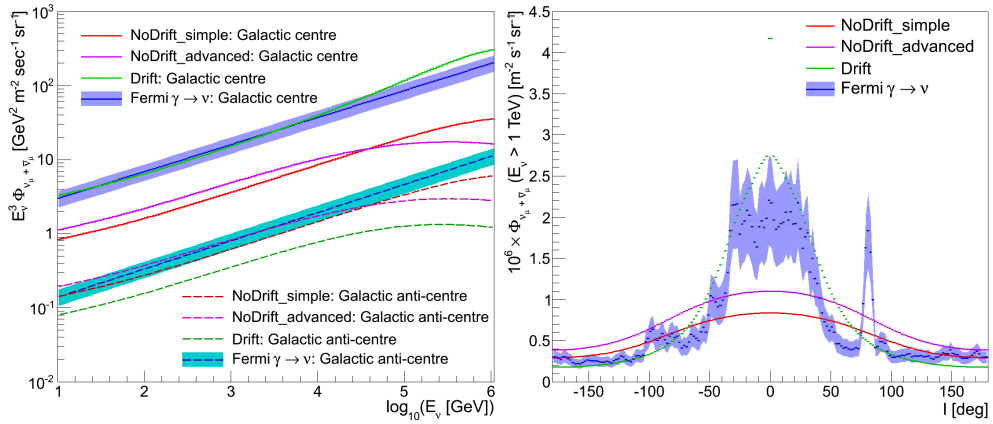

Figure 2.25: Neutrino fluxes for all models. LEFT: versus neutrino energy. RIGHT: versus Galactic longitude.

has not been taken into account and leads to an underestimation of the neutrino fluxes of the order of 10% (see section 2.2.2). Since the overestimation of the neutrino fluxes by not considering η^0-decays is of the same size, the combined effect is expected to be small compared to the total systematic error.

The result of the calculations can be seen in figure 2.25, in which the fluxes calculated in this way are compared to the theoretical fluxes calculated earlier (figure 2.16). The fluxes calculated in this way will be referred to as the 'Fermi $\gamma \rightarrow \nu$' model. Neutrino oscillations have been taken into account using equation 2.53. The blue band around the flux calculated from the Fermi data represents the total systematic error which consists of the combination of the uncertainty on the Fermi-LAT effective area and the uncertainty in the π^0-decay contribution. The systematic error is about 25% and is independent of the neutrino energy.

The agreement between the theoretical fluxes and the flux calculated here is reasonable. The flux from the Fermi $\gamma \rightarrow \nu$ model is similar to the flux from the Drift model, as can be seen from the left plot in figure 2.25. When comparing the longitudinal distribution, it can be seen that the Fermi $\gamma \rightarrow \nu$ fluxes are higher than the NoDrift fluxes in the inner Galactic plane and lower outside of it. The flux is less smooth than the theoretical predictions, due to the simplifying assumptions (such as cylindrical symmetry) made in the latter. In addition, the Cygnus region, which is a known source of diffuse γ-ray emission, is visible at a longitude of 80°.

The spectral indices obtained by the four models are similar. The spectral index of the diffuse Galactic neutrino flux is comparible to that of the cosmic ray flux, ranging from about 2.6 to 2.7, see also table 2.3 in section 2.4.3.

2.4 SIGNAL FLUX COMPARISONS

There are two types of background that are important for this analysis, which are, just like the signal, created in cosmic ray interactions. The target in this case is not the interstellar matter, but the atmosphere of the Earth. In these interactions, a so-called air shower is created, which contains pions, kaons, muons and a myriad of heavier hadrons. Muons are the dominant charged component at sea level, followed by protons [Grupen, 2005]. Some of these (higher energy) atmospheric muons also reach the detector, in which they can generate a signal. However, since muons cannot pass through the entire Earth, this background can be efficiently reduced by looking through the Earth. More details on this concept can be found in chapter 4.

The second type of background are neutrinos produced in the air showers, which are called atmospheric neutrinos. These neutrinos constitute the main background and will be described in more detail first.

2.4.1 *Atmospheric neutrinos*

Even though the mechanism that produces the atmospheric neutrinos is the same as that producing the diffuse Galactic neutrino flux, the neutrino fluxes are quite different. The atmosphere of the Earth consists mainly of nitrogen and its density is substantially higher than that of the Galaxy. Because of the low density in the Galaxy, all pions and muons produced there will decay and contribute to the diffuse Galactic neutrino flux. For atmospheric neutrinos, the main contribution comes from the pions and kaons, since most muons will reach the Earth before decaying. Furthermore, because of the higher density, most created particles will interact before decaying, thereby losing some of their energy. This results in a softer energy spectrum for the atmospheric neutrino flux compared to the diffuse Galactic neutrino flux. The spectral index of the former is about 3.7, compared to the 2.6 to 2.7 for the diffuse Galactic neutrino flux.

The atmospheric neutrino flux consists primarily of two contributions. For energies below about 50 TeV the conventional flux

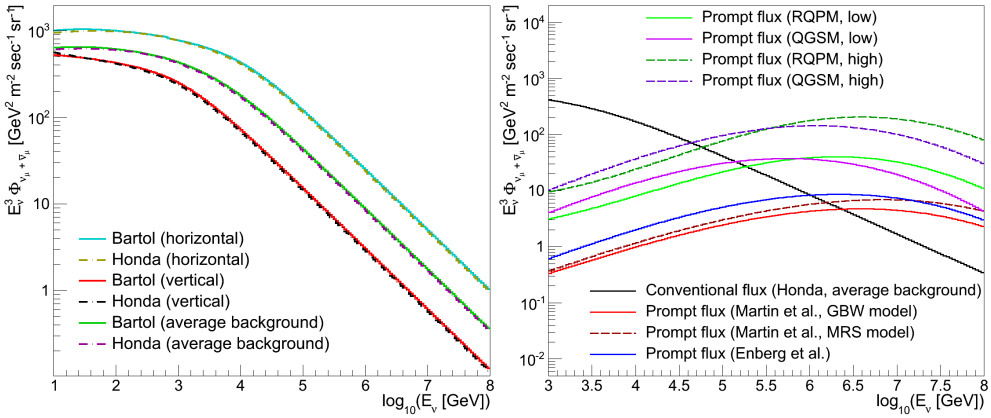

Figure 2.26: The atmospheric neutrino flux versus energy. LEFT: the conventional flux for several zenith angles. RIGHT: several models for the prompt flux.

(produced by pions and kaons as in reactions 2.42, 2.44 and 2.45) is the dominant component. For higher energies the prompt contribution takes over, which is due to charm-pair production ($D^{\pm}$, D^0, etc.). For an overview of the atmospheric neutrino flux, see the thesis of Palioselitis [2012].

The conventional flux depends on the zenith angle, since the path length through the atmosphere changes. It can be seen from the left plot in figure 2.26, in which the conventional neutrino flux is shown versus neutrino energy, that the horizontal (zenith $= 90°$) flux is higher than the vertical (zenith $= 0°$ and zenith $= 180°$) flux. The average background expected for the diffuse Galactic neutrino flux coming from the inner Galactic plane is also shown (the average zenith angle is about $110°$). The fluxes are shown for two frequently used models: the flux calculated by Honda et al. [2007] (called the *Honda*-flux) and that calculated by Barr et al. [2004] (called the *Bartol*-flux, named after the institute where two of the authors are affiliated to). The model predictions are very similar; the largest difference is about 6%. In the following the *Honda*-flux model is used as the conventional component of the atmospheric neutrino flux. The uncertainty on this conventional flux is about 7% at 10 GeV, 14% at 100 GeV and 25% at 1 TeV [Palioselitis, 2012].

Different models for the prompt neutrino flux are shown in the right plot of figure 2.26. The models from Martin et al. [2003]

and Enberg et al. [2008] are in agreement with each other within a factor of two, but there are also models that predict significantly higher fluxes (the RQPM and QGSM models in the figure, see [Palioselitis, 2012] for details). Recent results from the IceCube experiment, in which the prompt component is fitted using the observed neutrino events, seem to favour a low prompt neutrino flux [Aartsen et al., 2014].

The prompt contribution is not so important for this work, since the conventional flux constitutes the main background and the uncertainty on it contributes more than the difference between the prompt models. The flux model from Enberg et al. [2008] is used as the prompt component.

Concerning neutrino oscillations, a slightly different calculation has to be performed than for Galactic fluxes. Starting again from equation 2.50, the $\sin^2 \Delta_{ij}$ term can now not be averaged over. However, since $\Delta m^2_{32} \simeq 2.5 \cdot 10^{-3}\,\mathrm{eV}^2/c^4$ is substantially larger than $\Delta m^2_{21} \simeq 0.8 \cdot 10^{-4}\,\mathrm{eV}^2/c^4$, the latter mass splitting can be neglected, and the so-called two-flavour approximation can be used. The probability that a muon-neutrino stays a muon-neutrino can then be written as [Beringer et al., 2012]:

$$P_{\nu_\mu \to \nu_\mu} = 1 - \sin^2(2\theta_{23}) \sin^2 \left(1.27 \frac{\Delta m^2_{32}\,[\mathrm{eV}^2] L\,[\mathrm{km}]}{E_\nu\,[\mathrm{GeV}]} \right). \quad (2.62)$$

For energies above a few hundred GeV and neutrino travel distances of at most two times the Earth's radius ($2r_\oplus \approx 13000\,\mathrm{km}$), which are typical values of interest for this work, the muon-neutrino flux reduction is negligible.

2.4.2 *Signal compared to the background*

The diffuse Galactic neutrino flux is compared to the average atmospheric neutrino background in figure 2.27. The atmospheric neutrino background dominates over the signal for most of the energy range. In the direction of the Galactic centre, the diffuse Galactic neutrino flux rises above the background at an energy of about 40 TeV for the Drift and Fermi $\gamma \to \nu$ models, at about 250 TeV for the NoDrift_simple model and at about 1 PeV for the NoDrift_advanced model. For the other directions this happens for higher energies, since the signal flux is lower in these directions.

From figure 2.27 and the right plot in figure 2.25 it can be concluded that the optimal region to look for the diffuse Galactic

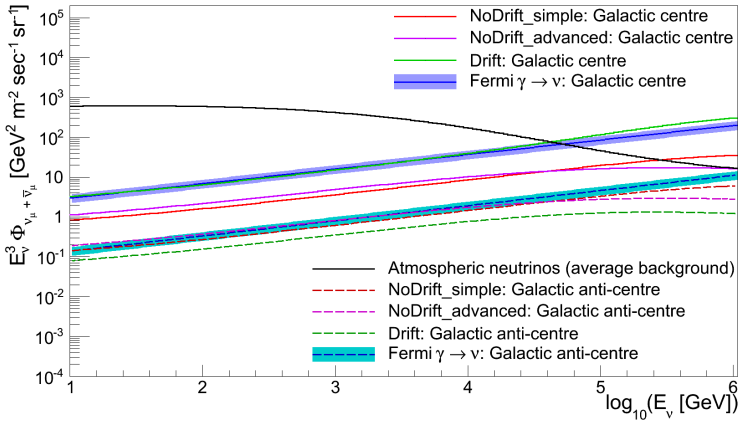

Figure 2.27: The diffuse Galactic neutrino flux for two different directions compared to the (average) atmospheric neutrino background versus neutrino energy.

neutrino flux will consist of the inner part of the Galactic plane and only events with energies above a few TeV should be selected.

2.4.3 *The Mediterranean sea versus the South Pole*

From the previous discussion it is clear that it is best to have a detector with a high visibility of the Galactic centre, or more generally the inner Galactic plane. The visibility $\mathcal{V}$ is defined as the percentage of time a given direction can be observed. Since neutrino telescopes use the Earth as a shield, this means that the source has to be below the horizon (i. e. only directions with $\theta \geqslant 90^\circ$ are considered). Using the fact that a given direction in Galactic coordinates will have the same local detector coordinates after exactly one sidereal day has passed, the visibility can be calculated as:

$$\mathcal{V} = \frac{\int_0^T \mathrm{d}t \; v(l, b, t)}{\int_0^T \mathrm{d}t}, \tag{2.63}$$

where $T = 23.9345\,\mathrm{day}$ is one sidereal day and with:

$$v(l, b, t) = \begin{cases} 1 & \theta(l, b) \geqslant 90^\circ \\ 0 & \theta(l, b) < 90^\circ \end{cases} \tag{2.64}$$

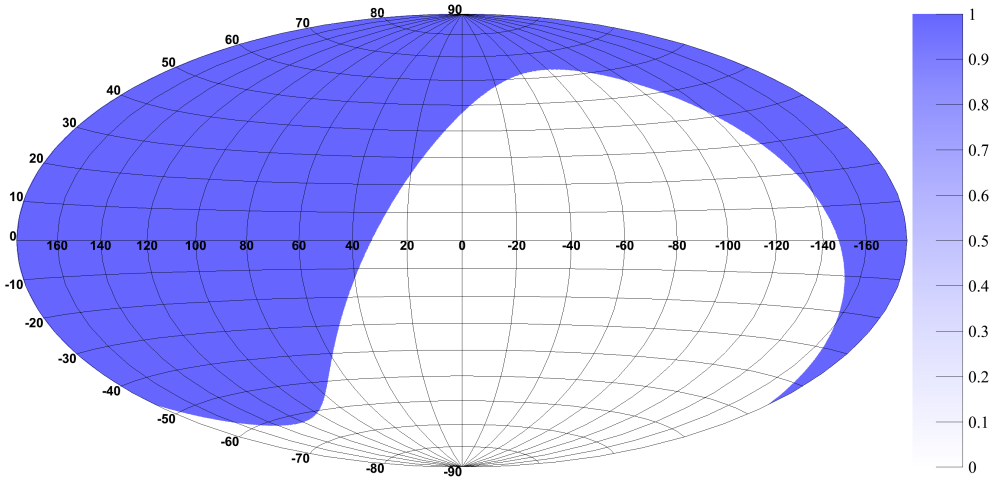

Figure 2.28: Sky-map of the AMANDA/IceCube visibility.

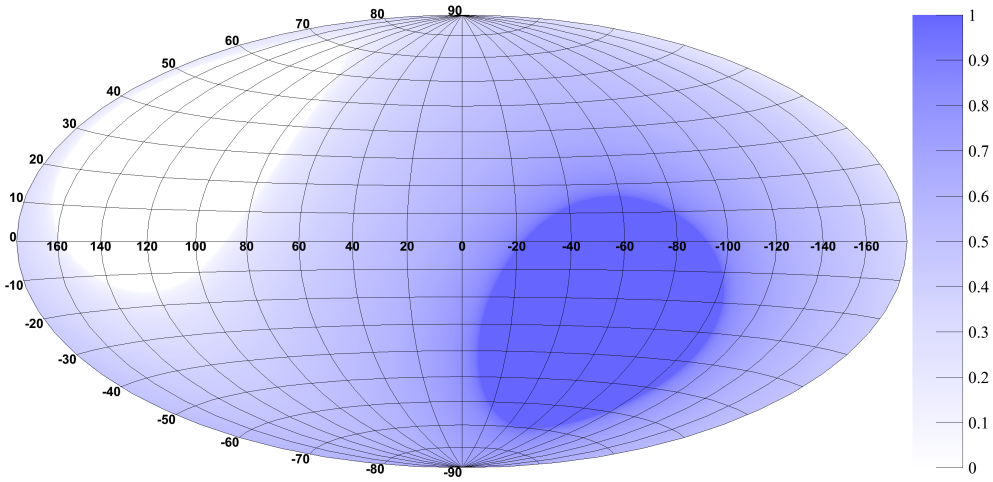

Figure 2.29: Sky-map of the ANTARES/KM3NeT visibility.

The visibility of AMANDA (and of IceCube[14]) is 100% for the Northern sky, which corresponds to Galactic longitudes between 33° and 213° for $b = 0°$. A sky-map of the visibility of AMANDA/IceCube is shown in Galactic coordinates in figure 2.28. The visibility of ANTARES[15] is diluted and is shown in Galactic coordinates in figure 2.29. The visibility sky-maps display one of the advantages of a detector in the Mediterranean sea compared to one on the South Pole for measuring the diffuse Galactic neutrino flux: the Galactic centre has a high visibility for the former (about 68% for ANTARES).

The diffuse Galactic neutrino fluxes averaged over the region $33° < l < 213°$; $-4.4° < b < 4.4°$, i. e. the region used by the AMANDA-II experiment to set their limit, are plotted in figure 2.30 versus neutrino energy. For comparison, the fluxes in the region $-39° < l < 39°$; $-4.5° < b < 4.5°$ are also shown, which is the region of interest for ANTARES[16]. The average flux in the ANTARES region is about a factor of 3 higher than in the AMANDA region, although this differs per model. In table 2.3 the average flux integrated above 1 TeV in the ANTARES region compared to that in the AMANDA region is summarised for the four models.

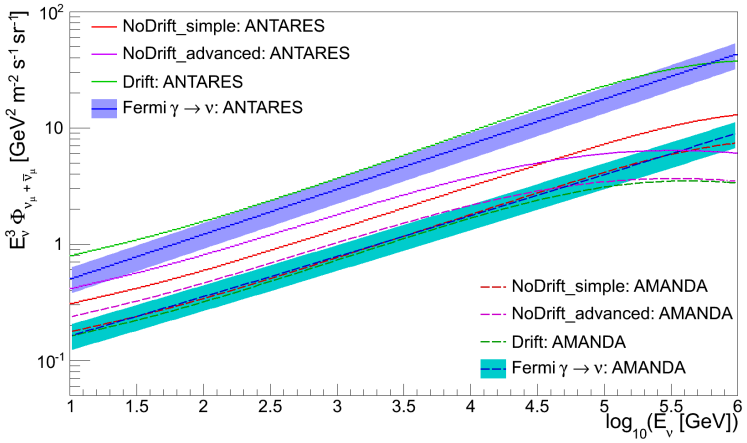

Figure 2.30: Average diffuse Galactic neutrino fluxes versus energy for the ANTARES and AMANDA regions.

Also shown in table 2.3 are the spectral indices for the four models, that have been obtained from a fit to the fluxes shown in figure 2.30 for a neutrino energy between $E_\nu = 100\,\text{GeV}$ and $E_\nu = 100\,\text{TeV}$. The spectral index for the NoDrift models is identical in both regions, since these fluxes just scale with the column density. For the other two models, the spectrum in the

[14] *Using the veto-technique, IceCube is also able to observe the Southern sky, which results in a different visibility than shown in figure 2.28. However, since IceCube can only observe very high energy neutrinos ($\gtrsim 100\,\text{TeV}$) coming from the Southern sky, this is not relevant for the current discussion.*

[15] *The visiblity of the future KM3NeT detector will be very similar.*

[16] *This is the region that is found to be optimal, see chapter 5.*

MODEL NAME	AVERAGE FLUX ANTARES REGION TO AMANDA REGION	SPECTRAL INDEX ANTARES REGION	SPECTRAL INDEX AMANDA REGION
NoDrift_simple	1.8	2.63	2.63
NoDrift_advanced	1.8	2.69	2.69
Drift	4.5	2.61	2.65
Fermi $\gamma \rightarrow \nu$	4.0	2.61	2.65

Table 2.3: Average flux above 1 TeV in the ANTARES region compared to that in the AMANDA region and spectral indices for the average fluxes from $E_\nu = 100\,\text{GeV}$ to $E_\nu = 100\,\text{TeV}$.

ANTARES region is slightly harder than that in the AMANDA region.

To complete the comparison of ice and water, it is important to mention the detection media themselves. More on this, and the optical properties (which are also different for the two detection media) can be found in the next chapter.